LHCb Collaboration

LHCb 2000-083 RICH
27^{th} August, 2000

Performance of a Multianode Photo Multiplier Cluster equipped with Lenses

V. Gibson, S. Katvars, S. Wotton
University of Cambridge
E. Albrecht, L. Eklund
CERN
S. Eisenhardt, F. Muhiem, S. Playfer
University of Edinburgh
A. Petrolini
University of Genova
S. Easo, A. Halley
University of Glasgow
G. Barber, A. Duane, D. Price, D. Websdale
Imperial College, University of London
M. Calvi, M. Paganoni
Universita degli Studi di Milano
J. Bibby, M. Charles, N. Harnew, J. Libby, J.Rademacker, N. Smale, S. Topp-Jorgensen, G.Wilkinson
University of Oxford
J. Baker, M. French
Rutherford Appleton Laboratory

Abstract

Studies of Multi–anode Photo Multiplier Tubes (MaPMTs), which are a possible photo–detector for the LHCb RICHes, are presented. These studies include those of a cluster of MaPMTs equipped with lenses at the SPS beam during the Summer of 1999. The read–out electronics used were capable of capturing the data at 40 MHz. Results on the effect of charged particles and magnetic fields on MaPMTs are also presented.

1 Introduction

This paper reports on the performance of Multi-anode Photo Multiplier Tubes (MaPMTs) for the detection of Čerenkov light in a prototype RICH detector. The MaPMTs are a possible choice[1] for the photo–detector to be used in the RICH detectors of the LHCb experiment [2] at the future Large Hadron Collider (LHC) at CERN. The performance studies presented here include, for the first time, those where the MaPMT data has been captured at 40 MHz, which is the interaction rate of the LHC.

The LHCb experiment is a dedicated B-physics experiment at the LHC. The detector is being optimised for the exploitation of the huge $b\overline{b}$ cross section in pp collisions at 14 TeV. This will allow high-precision measurements of CP asymmetries in B–decays to be made. Many of the sensitive decay modes have branching ratios that are of the order 10^{-5}. The particle identification provided by the RICH detectors allows the selection of pure data samples from which to measure the often small CP violation effects. For example, the $\pi - K$ separation offered by the LHCb RICH detectors is crucial for distinguishing the decay $B^0_d \to \pi^+\pi^-$, which is sensitive to the CKM-angle α, from other two–body decays: $B^0_d \to K^+\pi^-$, $B^0_s \to K^+\pi^-$ and $B^0_s \to K^+K^-$.

LHCb will have two RICH detectors to allow particle identification over a momentum range of 1 to 150 GeV. The upstream RICH1, which is located after the vertex detector, has two radiators: 5 cm of aerogel and 95 cm of gaseous CF_4 radiator. These two radiators allow RICH1 to provide $\pi - K$ separation over a momentum range from 1 to 70 GeV with in an acceptance of 10 to 330 mrad from the beam axis. The larger upstream RICH2, which is located after the main tracking detector, has a single 1.8 m long radiator of C_4F_{10} gas. RICH2 has extended $\pi - K$ separation up to a momenta of 150 GeV with in a reduced acceptance of 10 to 120 mrad.

In both cases the Čerenkov photons produced in the radiators are initially reflected off a tilted spherical mirror. In RICH1 the reflected photons fall directly onto an array of photo–detectors in the focal plane of the mirror. In RICH2 there is an additional reflection off a flat mirror before the photo–detector plane; this allows for a larger focal length (and hence larger image) with a reasonably compact design.

For the two detectors combined an area of 2.9 m^2 has to be instrumented with photo–detectors. The photo–detectors are required to be both efficiently single photon sensitive (as few as ~ 7 photons are expected to be detected in RICH1 for an average ring from the aerogel radiator) and spatially precise to a few millimetres. Furthermore, the device and accompanying electronics must have a fast enough response to be read–out in 25 ns, the time between LHC bunch crossings.

Single MaPMTs and an array of 3×3 MaPMTs have been tested in a RICH prototype in a beam at the CERN SPS facility. In order to reduce the losses of photons in the dead areas at the edges of the MaPMT, which corresponds to about 50% of the total area, the MaPMTs have been equipped with lenses. Pipelined read–out electronics, which were compatible with the LHC 25 ns bunch crossing interval and partially satisfied the requirements of the LHCb pipelined trigger and read–out architecture, have been tested for the first time on a RICH prototype. Also the effects of two potential hazards in a real detector environment have been investigated: the effect of charged particles traversing the tubes and the lenses and the impact of different strength magnetic fields on the performance of the tubes. For the magnetic field tests the possibility of shielding the tubes against such fields was also studied.

The main aim of the tests was to demonstrate that the MaPMT is a viable photo–detector for the LHCb RICH system. These tests fall into three main areas:

- the demonstration of the performance of the MaPMTs, both individually and in an array, with and without lenses,
- the tubes operation with pipelined read–out electronics,
- and the functionality of the tubes in a real detector environment.

Each of the above topics is reported upon below. In addition, laboratory tests of aspects of the hardware are presented, in particular those concerning the pipelined electronics.

[1] The current baseline solution is the Pixel Hybrid Photo–diode Detector (HPD), studies of which are reported elsewhere [1]. A final photo–detector choice will be made at the end of the year 2000.

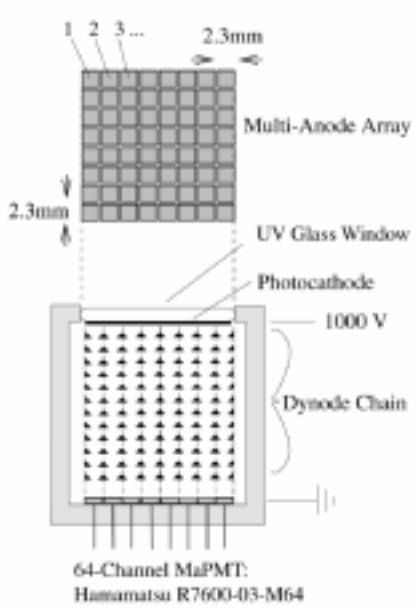

Figure 1: Sketch of a multianode photomultiplier tube.

The organisation of this paper is as follows. Section 2 will contain a description of the hardware used in both the test beam and in the LED scanning facilities. The lenses and the pipelined electronic read–out system will be described in detail. In Section 3 the test beam results with respect to Čerenkov photon counting with and without lenses, will be presented. In addition, the performance when the angle of incidence between the incoming Čerenkov photons and the detector plane is varied are investigated. In Section 4 the results of laboratory tests of the tubes and electronics using LED scans will be reported. The results are compared to a simulation of the RICH prototype. Section 5 and Section 6 give the results of the charged particle and magnetic field studies respectively. Finally, a summary and conclusions are given in Section 7.

2 Hardware characterisation

2.1 Multianode Photomultiplier Tubes

The multianode photomultiplier tube (MaPMT) consists of an array of square anodes each with its own metal dynode chain incorporated into a single vacuum tube to amplify the photoelectrons. The densest pixelization available, 8×8 pixels, provides the spatial resolution required for the LHCb RICH detector. Figure 1 shows a schematic of the MaPMT. The dynode structure is separated into 64 square pixels of 2.0 x 2.0 mm^2 area, separated by 0.3 mm gaps.

The 64-pixel MaPMTs are commercially available and have been tested by LHCb in 1998 [3]. Since then the manufacturer, Hamamatsu, has provided some modifications which better match our specifications. The MaPMT R7600-03-M64[2] described in this paper has a 0.8 mm thick UV-glass window with a semi-transparent photocathode deposited on the inside. The threshold for the light transmission through the UV-glass window is at a wavelength of 200 nm. The photons are converted into photoelectrons in a Bialkali photocathode. The quantum efficiency of the MaPMT, measured by Hamamatsu, is plotted versus the wavelength of the photons in Figure 2. The quantum efficiency has a maximum of 22% at 380 nm. For each pixel the photoelectrons are focused onto a 12-stage dynode chain (see Table 1) and multiplied through secondary emission. The mean gain of the MaPMT is about 3×10^5 when operated at a voltage of 800 V. Nine MaPMTs have been purchased, preselected such that the average gain of the tubes varies not more than a factor of two. A study of the variation of gain for the 64 pixel within one tube will be presented in this paper.

The geometrical coverage of the MaPMT, i.e. the ratio of the sensitive photocathode area to the total tube area including the outer casing is only $\sim 48\%$. This fraction can be increased by placing a single lens with one refracting and one flat surface in front of each MaPMT. In the thin lens approximation a single refracting surface with radius-of-curvature R has a focal length

$$f = \frac{R}{1 - 1/n}$$

where n is the refractive index of the lens material. Figure 3 shows a schematic view of such a

[2]With respect to its predecessor, the R5900-00-M64, the borosilicate window is replaced by a UV-glass window which increases the integrated quantum efficiency by 50%. In addition, a flange of 1 mm size around the MaPMT is removed, thereby improving the packing fraction by 14%.

Dynode	1	2	3	4	5	6	7	8	9	10	11	12	Anode
R in $[10^5$ k$\Omega]$	3	2	2	1	1	1	1	1	1	1	1	2	5

Table 1: Resistances R in $[10^5$ k$\Omega]$ in front of each dynode.

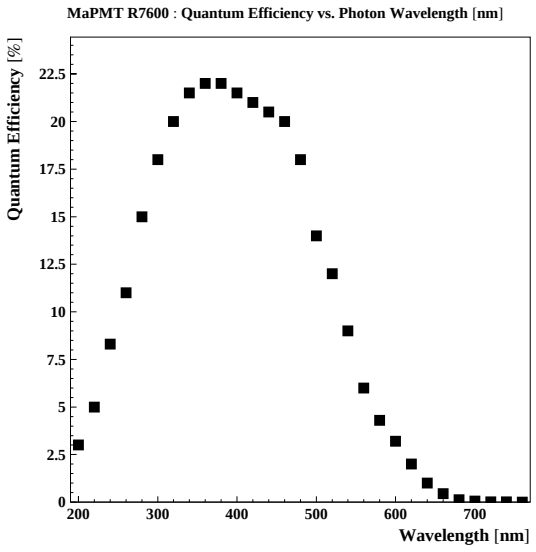

Figure 2: Quantum efficiency of the MaPMT R7600-03-M64 as a function of wavelength, measured by Hamamatsu.

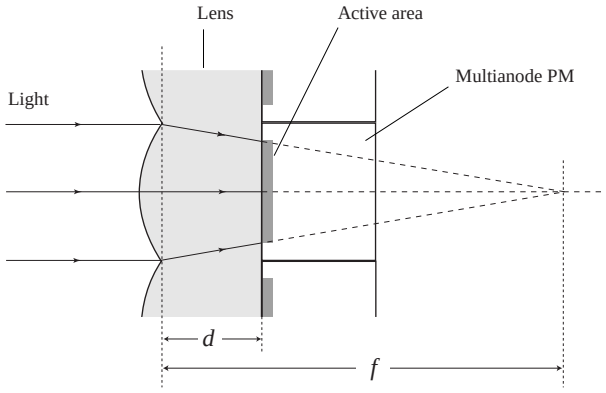

Figure 3: Schematic view of lens system, in front of the close-packed photomultipliers (side view). The focusing of normally incident light is illustrated. The full aperture of the lens is focused onto the sensitive area of the MaPMT.

lens system in front of the close-packed photomultipliers. If the distance d of the refracting surface to the photocathode is chosen to be equal to R the demagnification factor is $(f-d)/f \approx 2/3$. Over the full aperture of the lens light at normal incidence with respect to the photodetector plane is focused onto the photocathode, thus restoring full geometrical acceptance. The demagnification resulting from this lens configuration is illustrated in Figure 4. This demonstrates that the pin cushion distortion is small compared to the pixel size. The focusing is also quite independent of the angle of incidence of light. Nine quartz lenses, one for each MaPMT have been purchased. Their dimensions are square width of 26$\times$ 26 mm^2, R =25 mm and maximum height 24 mm.

2.2 Electronics

The tests involving individual MaPMTs were performed using a read–out chain of CAMAC amplifiers and ADCs [3]. For the beam tests of the 3×3 array of MaPMTs a new pipelined electronic read–out system was used and it is shown schematically in Figure 5. An overview of the system will follow before several of the components (which are italicised) will be described in more detail.

Nine MaPMTs were mounted in a 3×3 array on a *bleeder board* unit, which positioned the photo–cathodes of the MaPMTs in the focal plane of the mirror. The output signal channels in the back plane of the bleeder board were coupled to the *front–end boards* via *kapton cables*. Each front–end board multiplexed the analogue signals from one or two MaPMTs and was the carrier for the front–end ASIC (Application–Specific Integrated Circuit), the *Analogue Pipeline Voltage MSGC (APVm)* [4, 5, 6]. The APVm shaped, am-

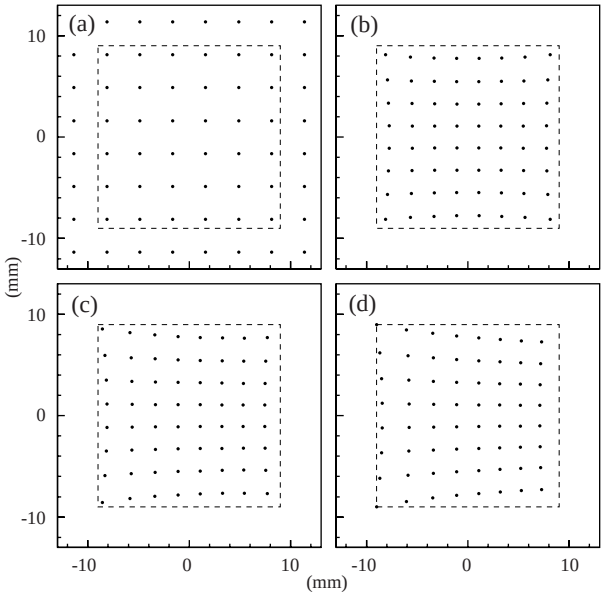

Figure 4: Impact points of a bundle of light rays incident on the entrance window of a multi-anode photomultiplier tube: (a) with no lens, (b-d) with a lens; (b) is for normally incident light, (c) and (d) are for an angle of incidence of 200 mrad and 400 mrad in the horizontal plane, respectively. The solid (dashed) line indicates the the total (sensitive) area of the tube.

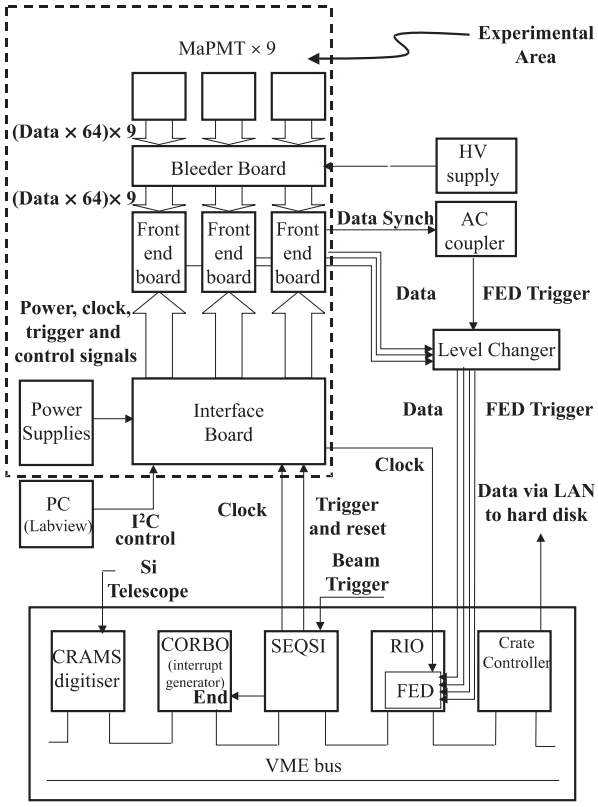

Figure 5: A block diagram of the electronic read–out and data acquisition systems. The components within the dashed box were in the experimental area.

plified, buffered and multiplexed the input signals. The front–end boards were then coupled to a single *interface board*, which fanned–out the power, the trigger signals, the clock and the Philips I^2C control signals [7] for the APVm. The analogue pipeline signals from the APVm and the accompanying output data synch were routed directly to the Front–End Digitiser (FED) and the rest of data acquisition system, which is described in Section 2.3.

2.2.1 Bleeder board

The bleeder board provided the mechanical support and dynode chain resistor network for up to 16 MaPMTs in a 4×4 array. The board also adapted the MaPMT anode feedthrough pitch of the 1024 data channels to the Pin Grid Array (PGA) pitch of the kapton cable. To achieve the minimum dead space between MaPMTs, while providing adequate High Voltage (HV) isolation, careful layout of the board was required. In particular, the relative orientation of the MaPMTs and the size and layout of the dynode chain resistors were optimised to minimise the voltage gradients between conductors. The bleeder board was constructed as two separate parts: the HV distribution board and the pitch adapter board. These were then assembled as a single unit using an array of soldered interconnect pins.

2.2.2 Kapton cables

The kapton cables were used to couple the 8×8 output PGA for each tube, in the backplane of the bleeder board, to the front–end board. The kapton cables can be seen in Figure 6. The kapton cable from one MaPMT was coupled to two 40–

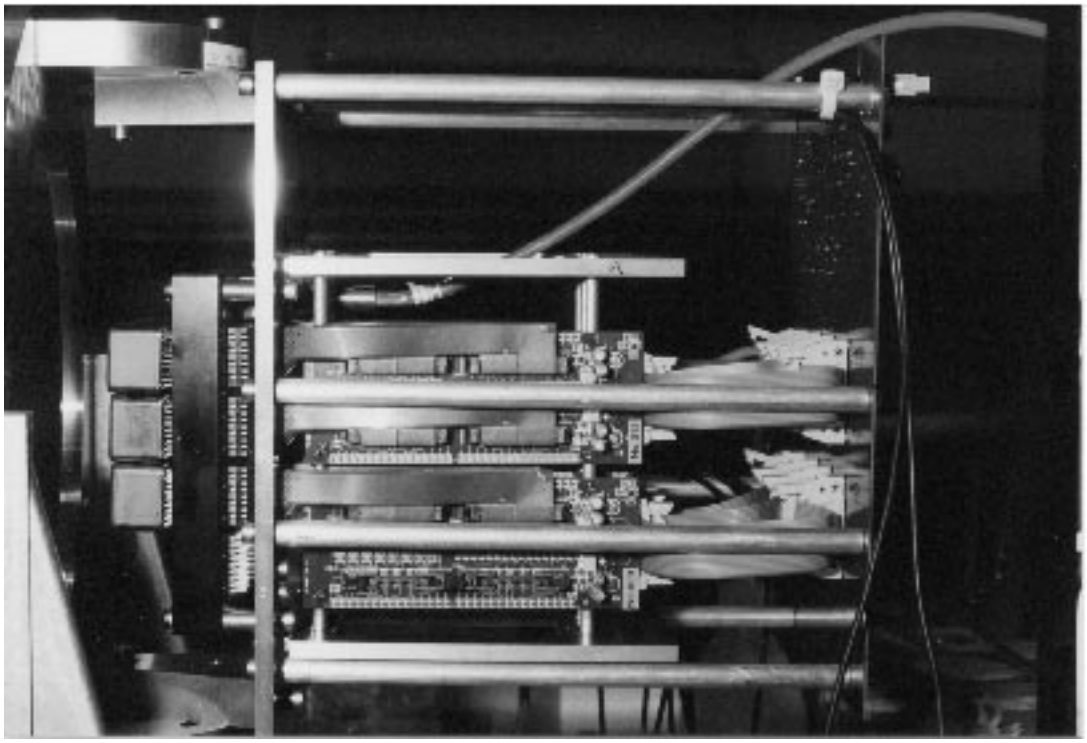

Figure 6: A photograph of the MaPMT array, bleeder board and front–end electronics along with the mechanical support used in the test beam. The profile of 3 of the MaPMT tubes can be seen plugged in to the bleeder board on the left hand side of the photograph. The output pins in the back plane of the bleeder board are coupled via kapton cables to two front–end boards. The interface board is on the right–hand side of the photograph and it it's plane is perpendicular to that of the front–end boards. The interface board is connected to the front end boards via ribbon cable plugged in to IDC connectors. *the resolution of this photograph can be improved but to keep the .eps file size managable the resolution is currently degraded*

way SAMTEC connectors (64 data channels and 16 ground lines) on the front–end board.

The cables were flexible printed circuits with the tracks laid on one side of the kapton and a ground plane on the reverse. A cable was composed of 4 strips of kapton; each strip coupled 2 columns of MaPMT output pins to half the channels of one SAMTEC connector. Each layer of kapton was coated with an insulator to isolate it from it's neighbouring layers. To map the 4 layers to the two SAMTEC sockets on the front–end boards the pieces of kapton differed in length by up to a factor of two. These differences in the track lengths for the MaPMT data channels led to differing stray capacitance contributions to the attenuator network on the front–end board, which is described in Section 2.2.3. These stray capacitance values varied between 14 to 30 pF, which led to differences between channels in the attenuation factor of the AC–coupler.

2.2.3 Front–end board

The layout of the front–end board is given in Figure 7. The main components on the board are the AC–coupler network and the APVm ASIC. The APV ASICs were designed for use with silicon strip detectors or Micro Strip Gas Chambers (MSGCs) which produce signals approximately 10 times smaller than those from a MaPMT. There-

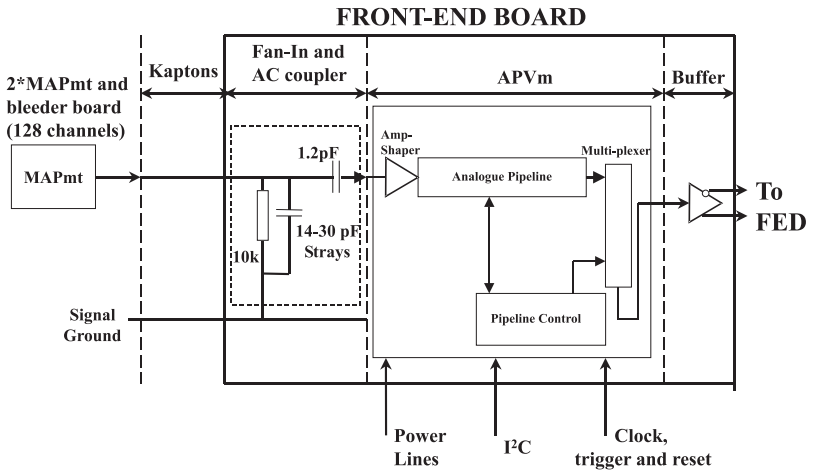

Figure 7: A schematic of the front–end board which carries the APVm ASIC.

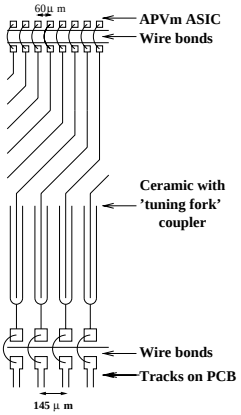

Figure 8: A section through the AC–coupler network.

fore, the MaPMT signals had to be attenuated to be within the dynamic range of the APVm. An AC–coupler was used to attenuate the signals. The coupler was made from a ceramic base on which gold tracks were laid. The a schematic of a section through the AC–coupler is given in Figure 8, which shows the 'tuning fork' capacitive coupling used.

The 128 active input signals were routed within a multi–layer Printed Circuit Board (PCB) from the 4 SAMTEC sockets to pads adjacent to one edge of the AC–coupler. The 128 PCB pads were attached to the AC–coupler inputs with wire bonds pitched at 145 μm. The outputs from the AC–coupler were connected to the APVm ASIC inputs using wire bonds pitched at 60 μm.

The front–end board also carried further components to perform three additional functions: (i) there were buffers to drive the output signals through 10 m of cable to the data acquisition system outside the experimental area, (ii) there were components to set unique addresses for each front–end ASIC, so that the control voltages and currents could be set individually via an I^2C control link and (iii) a switch to power cycle and thus reset the APVm.

2.2.4 APVm

The APVm [6] is one of the APV series [4, 5] of radiation hard front–end ASICs, which have been designed for the read–out of the CMS inner detector [8]. The APVm has been fabricated using the Harris AVLSIRA bulk CMOS process [9]. These ASICs have been previously used in a beam environment for the read–out of silicon–strip detectors [4].

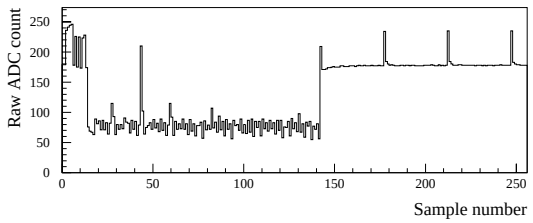

Figure 9: An example of the analogue output of the APVm ASIC. The header and pipeline address bits can be seen at the left–hand side of the frame. A signal can be seen approximately one quarter of the way along the data frame. Also smaller signals are situated at ±16 samples either side of the principle peak; these are a consequence of cross–talk which is discussed in Section 3.

In the test–beam readout system the APVm ASIC, running at 40 MHz, sampled the 128 input analogue signals every 25 ns. The signals were stored in a pipeline structure which allowed a maximum first level trigger latency of 3.2 μs. The pipeline structure contained 160 cells, including buffer storage for events awaiting read-out, and was compatible with a maximum first level trigger rate of 1 MHz.

Once the APVm was triggered the event sample pipeline address, corresponding to the latency, was stored in a FIFO; up to 16 events could be stored before the FIFO overflowed. At a variable time later, which depended on the events position in the pipeline and the number of events waiting to be read–out, the ASIC multiplexed the 128 signals into one analogue data output. The analogue output was cycled out of the ASIC at half the sampling rate (20 MHz). Preceding the 128 samples there were a further 12 samples which were logical levels internally set by the ASIC: 4 bits signalled the start of the analogue output and whether the ASIC was in error for an event, and the remaining 8 bits indicated the pipeline address at which the data were stored. The whole analogue data frame was 7 μs in length. An example of the analogue output of the APVm is given in Figure 9. Further details of the pipeline control logic can be found in [6] and the references therein.

Synchronous to the data output there was a second output which changes level when a data frame was being read–out. This data synch returned to the original level when the complete data frame had been output, as illustrated in the fifth line of the timing diagram given in Figure 10. This was used to trigger the data acquisition system as described in Section 2.3.

The APVm ASICs were not designed to meet the requirements of the LHCb trigger and read–out architecture. In particular, (i) the 1:128 multiplexing of the analogue input signals at 20 MHz precludes operation at the first level trigger rate of 1 MHz [10] and (ii) a signal return–to–zero within 25 ns is only possible in the de–convolution mode of APVm operation [4], which requires 3 consecutive samples for the algorithm, and therefore prevents triggering on consecutive events. Nevertheless these tests provided an important indication that the use of MaPMTs will be compatible with the operation of the LHCb RICH following the completion of other front–end ASICs [11, 12], which are currently under development and which address both these issues.

2.2.5 Interface Board

The interface board fans–out the LVDS (Low Voltage Differential Signalling) trigger and clock signals, which were generated by the SEQSI [13][3] VME module, to the front–end boards. Furthermore, it distributed the ±2 V and ±5 V power supplies required to operate the APVm and the buffers on the front–end board respectively.

The control of the bias voltages, shaping currents, latency, operation and calibration modes of the APVm, was done using the Philips I^2C protocol. The control signals were generated on a PC using a Lab-View interface to drive an I^2C PCI–card. An I^2C bus extender[4], placed on a separate card, was used to allow the signals to be driven over 10 m of cable into the experimental area. The I^2C signals were fanned–out to the front–end boards by the interface board. The I^2C signals generated at the PC may have been susceptible to ground loops and power surges related to the mains supply; therefore, to protect the front–end ASICs the I^2C signals were opto–coupled on to the board.

[3]The original ECL drivers were replaced by LVDS drivers in the SEQSI.

[4]Philips P82B715.

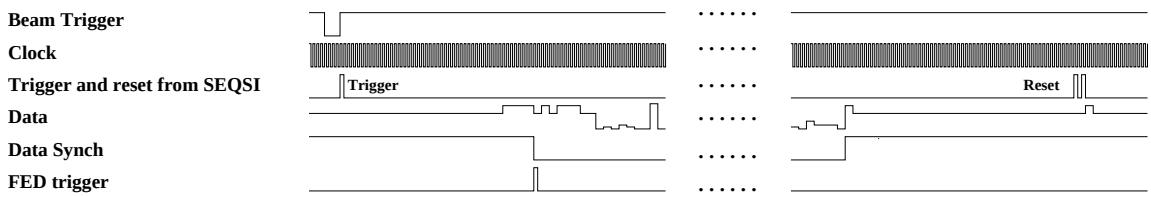

Figure 10: The timing diagram for the pipelined electronic read–out and data– acquisition system.

2.3 The data acquisition system

The main components of the VME based data acquisition system are shown in Figure 5. Data were generated from three sources: the nine MaPMTs, the silicon beam telescope and the trigger scintillators. The event size is dominated by the non–zero–suppressed MaPMT data which amounted to about 1.5 kByte per event. The acquisition system was capable of sustaining a trigger rate in excess of 1 kHz for the 1.7 s duration of the SPS spill.

The beam trigger was formed from the coincidence between the four scintillators in the beam line. Any further beam triggers were gated out for the remainder of the read–out cycle. The control of the front–end ASIC was performed using the outputs of the SEQSI programmable front–end control module [13]. For times outside the read–out cycle of the data acquisition system the SEQSI was in an 'idle loop', where no signals were sent to the front–end boards, apart from the continuous 40 MHz clock shown in the second line of the timing diagram in Figure 10. Once the NIM based trigger logic had made a positive decision a pulse (NIM type) was sent to the SEQSI to initiate the read–out command sequence. The beam trigger signal is shown in the first line of the timing diagram in Figure 10. The SEQSI then produced a 25 ns wide LVDS pulse to trigger the front–end ASIC, which marked the event in the pipeline to be readout; this is shown in the third line of the timing diagram in Figure 10.

The critical aspect of the data acquisition system timing was the correct determination of the trigger logic latency. This was done by the simultaneous pulsed emission of light from LEDs positioned at the beam entrance to the RICH prototype vessel and within one of the scintillators used in the trigger[5]. This imitated the beam conditions of Čerenkov radiation in the RICH vessel and charged particle causing scintillation light in the beam counters respectively. The latency of the ASICs was then varied in 25 ns steps, using the I^2C control circuit, until the maximum signal was observed in the APVm output.

The six APVm ASICs each produced an analogue data output which was digitised using the Front–End Digitiser (FED). The FED is a PCI Mezzanine Card (PMC) which was affixed to a VME based motherboard and processor unit[6]. The FED PMC was a prototype module for the read–out of the CMS inner tracker [14, 15]. The front–panel of the CMS FED PMC has 8 analogue input data channels, a trigger and a clock input. The data from the front–end boards were both level shifted and amplified, to fall within the dynamic range of the Flash ADCs (FADCs) on the FED PMC, by a separate level changing board.

The 40 MHz clock input was taken from the interface board; this was done to preserve the correct phase relationship between the clock and trigger input signals to which the FED PMC was sensitive. The trigger was required to be an LVDS signal of width less than 25 ns. This was created from the data–synch by AC coupling it's front–edge and then converted this pulse signal to LVDS on the FED level changing board.

Each analogue input to the FED was being continually digitised by the 9 bit FADCs at 40 MHz. Once a trigger was received the data for 256 samples were stored in a Dual Port Memory (DPM). These samples included the 12 header bits and 128 channel samples[7]. The FED was programmed to

[5]For this calibration the trigger logic was reconfigured to require a signal in this scintillator alone.

[6]CES RIO, model No. 8061.

[7]As the FED was operating at 40 MHz and the data from the APVm's were being cycled out at 20 MHz, the FED was configured to take every other sample to reduce the event size by a factor of two.

act in a 'digital scope' mode, which means that each individual event was read–out and no sparsification of the data was performed.

At the end of the read–out sequence an APVm reset pattern was asserted by the SEQSI, on the APVm trigger output, to clear the pipeline and reset the FIFO. Later, an 'end–of–readout' signal was generated at one of the SEQSI NIM output channels. This signal triggered the assertion of a VME interrupt using an interrupt generator module [8]. In response to this interrupt, a handler running in the read–out processor then copied the data from the FED PMC event buffers into the processor's local memory, before resetting the readout sequence and the clearing the trigger veto.

Event data were accumulated in the read–out processor's local memory during the SPS spill and were transferred via 100 MBit/s Ethernet connection to the mass storage device during the inter–spill gap.

2.4 Experimental setup for beam tests

The charged particle beam tests were carried out in the X7b beam at the CERN SPS. The beam was tuned to provide negative particles (95% pions) with momenta 120 ± 1 GeV/c. The experimental setup included scintillation counters and a silicon pixel telescope to define and measure the direction of the charged particles, a vessel which contained CF_4 gas radiator, a spherical mirror to focus the Cherenkov light and the MaPMT photon detector cluster. A schematic diagram of the setup is shown in Figure 11. The components are briefly described below and a more complete description can be found in reference [16].

The beam telescope comprises 3 planes of silicon detectors, each segmented into a 22×22 matrix of 1.3 mm square pixels. The pixels were read out using the Viking VA2 ASIC [17]. This is a 128-channel amplifier-shaper-multiplexer chip, four of which are mounted on each telescope plane.

The Cherenkov vessel is a full-scale prototype of the LHCb RICH1 detector. Charged particles enter the radiator volume along a tube of 90 mm internal diameter and intersect the centre of a spherical aluminized-glass mirror which is tilted by 18° to the beam axis. The plane of the MaPMT array is 1143 mm from the mirror centre. The mirror has a diameter of 112 mm and a focal length of 1117 mm. Its reflectivity has been measured [18] to be 90% at 600 nm, falling to 70% at 200 nm. The mirror is mounted on micrometer screws, fixed to the back plate of the vessel. These allow fine adjustments of the mirror tilt to reflect Cherenkov photons onto different regions of the photodetector array.

The Cherenkov radiator is CF_4 gas contained within a volume of length 1000 mm between the beam entrance window and the mirror. The gas is supplied at high pressure, via a recirculation system [3] to the vessel. The absolute pressure in the vessel could be set and stabilized by the system over a wide pressure range from $100 - 1200$ mbar. Throughout data taking, gas pressure and temperature, watervapour and oxygen concentrations were monitored. These were used for correcting the CF_4 refractive index, which has been parameterised as a function of wavelength at STP [19].

Between the mirror and the photon detectors the radiator vessel is sealed using a 25 mm thick fused silica plate. Initial tests verified that the loss of Cherenkov light resulting from transmission through this plate was 7%, consistent with that expected due to reflection.

The fused silica lenses described in 2.1 were close-packed and mounted close to, but not in optical contact with, the photocathode windows of the 3×3 array of MaPMTs. A micrometer screw allowed the position of the lens array to be displaced sideways by ± 5 mm with respect to the photocathodes. The overall photodetectorassembly could be rotated with respect to the incident Cherenkov light, though unless otherwise specified, most data were collected at normal incidence.

The numbering scheme used throughout this article for the tube, boards and pixels is shown in Figure 12.

2.5 Monte Carlo Simulation

A detailed simulation program of the experiment was developed, which is described in detail in [18, 3]. The refractive index index of the CF_4 radiator as a function of the photon wavelength is obtained from the parametrization used in [19], and is identical, as well as the measured mirror reflectivity, to the values given in [3].

[8] CORBO, CES RCB8047.

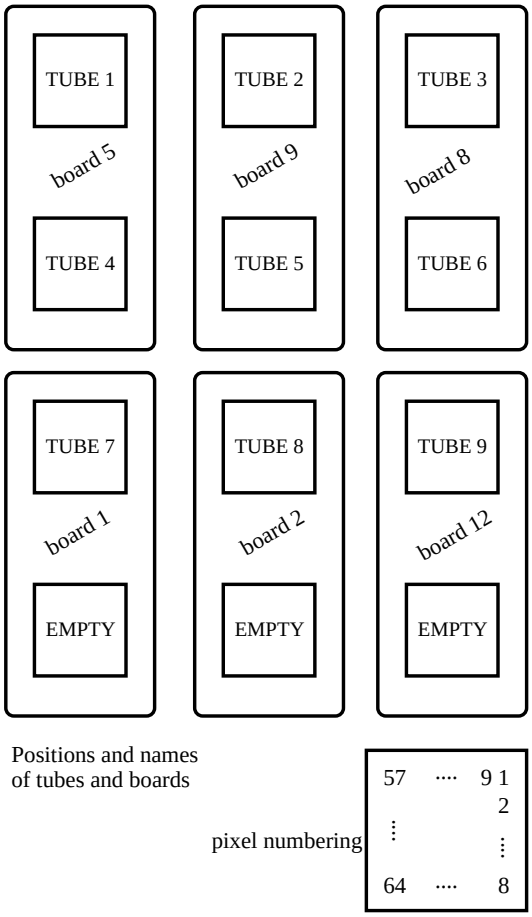

Figure 12: The following numbering scheme is used throughout the text (shown in the physical position on the detector plane, as seen from the mirror)

The program also simulates the MaPMTs as described in Section 2.1, including the effects of lens focusing (Figure 3), the geometry of the detector surface, (Figure 1) and the quantum efficiency of the MAPMTs, as measured by Hamamatsu[9] (Figure 2). A detailed electronics response (including the dynode chain) is not simulated, instead the signal loss at the first dynode and below the threshold cut is estimated from the data and then, averaged tube by tube, subtracted from the simulated photon counts.

[9]MAPMTs were manufactured by Hamamatsu Photonics, Japan.

2.6 LED scanning facilities

Further tests of tubes and the electronic read–out were performed using LED scanning facilities. Two such facilities were used. The most significant difference between them was the read–out electronics. One was instrumented with a CAMAC based read–out chain alone; the other could be instrumented with either a pipelined or a CAMAC based read–out chain. The general features of both facilities are described below.

The MaPMT were protected from extraneous light by a dark box housing. All cabling was brought into the box via feedthrough connectors, which were isolated from the frame of the box to reduce ground loops. The tube was supported and clamped in a silicon resin bonded fibre block. This provided insulation of the MaPMT casing, which was held at the bias potential, to prevent current leakage across the window.

The light source used was a blue 470 nm LED with a maximum luminosity of 1000 mcd and a view angle of 15°. The pulsing of the LED was performed using a FET circuit which provided a switching rate of 10 kHz with a pulse duration of approximately 10 ns. The LED was mounted externally and coupled in to the dark box using a monomode fibre. This was done for two reasons: to restrict the light pulse to a narrow light spectrum with a Gaussian distribution and to minimise the spot size from the the end of the fibre by reducing abberations. To reduce the LED spot size at the MaPMT window a sequence of lenses both at the entry and the exit. The lens system is described in Figure 13. The width of the light spot from the fibre at the MaPMT window was 50 μm or 100 μm depending on the focussing system. The light distribution was measured using a CCD camera.

The MaPMT and the fibre tip were both mounted on a motorised stages. The stages could be positioned with a resolution better than 5 μm which allowed precise scans over the MaPMTs acceptance. A stepper motor driver, interfaced to a PC, was used to control the stages.

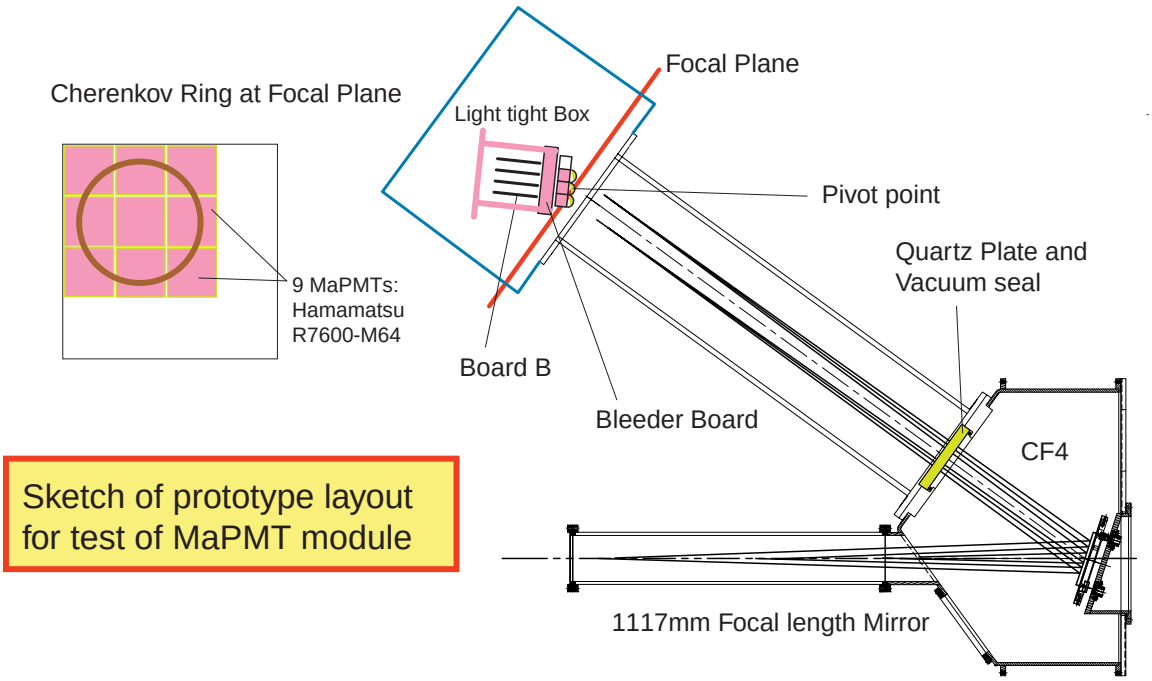

Figure 11: A schematic of the beam test setup.

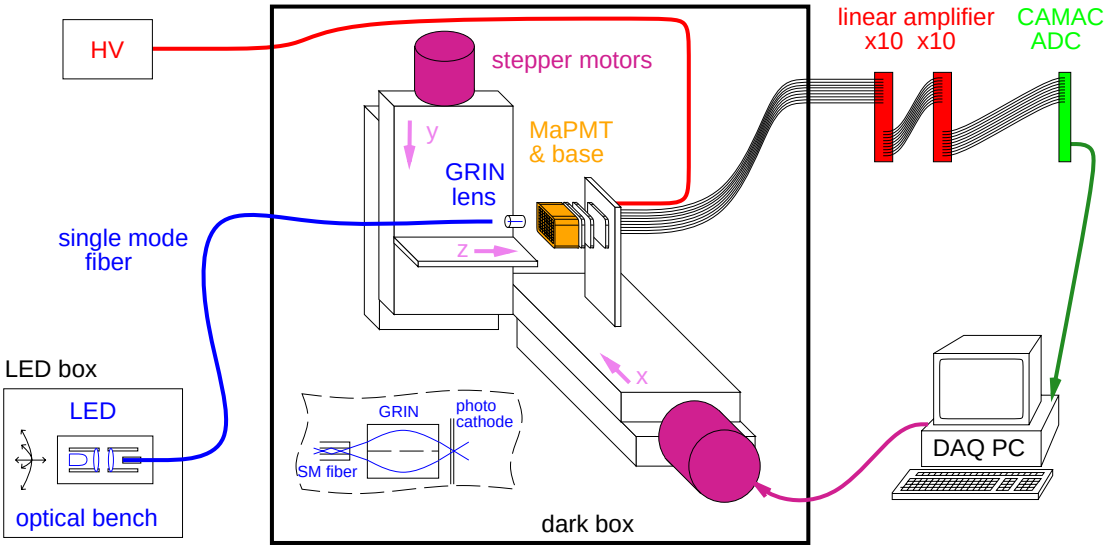

Figure 13:

Figure 14: Common-mode subtraction

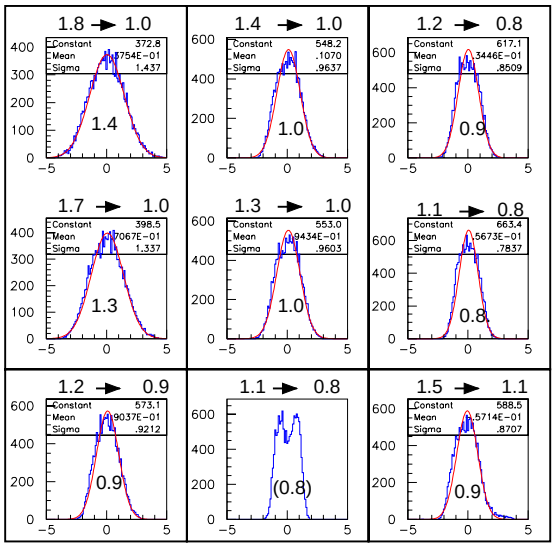

Common mode calculated and histogrammed for 1.3k events MaPMT by MaPMT. The histograms are ordered in the same way as the tubes on the event display (as seen from the mirror position). On top of each histogram the average pedestal width before → after common mode subtraction is printed. The numbers inside the histograms are the σ of the Gaussian fit (for tube 7: rms). Tubes on the same board (inside the same box) show, as expected, the same common mode behaviour.

(I'll have to re-check ratio (1%) for the ±8 xtalk)

Figure 15: The following types of cross talk were identified

:

source	who talks	ratio
Symmetric cross-talk		
1a) ceramic fan-in	apv input number $x \leftrightarrow x \pm 1$	0.15
1b) kaptons??	pixel number $x \leftrightarrow x \pm 8$	0.011
Asymmetric cross-talk		
2a) apv-chip	apv-sample $y \rightarrow y - 1$	0.33
mainly on board 9 and 12 (ratio from those boards).No next-to-nearest neighbour xtalk i.e. no $y \rightarrow y - 2$. See also fig 10, section 2.2		
2b) apv-chip	apv-sample $y \rightarrow y + 2$	0.034
mainly on board 2 (ratio only from board 2)		

'ratio' is the average pulse height ratio $f_{x,y} = h_x/h_y$ with h_x = pulse height in the talked-to pixel and h_y = pulse height in the talking pixel. Figure 18 shows scatter plots of pulse heights of pixels related by different types of cross talk.

3 Testbeam Performance

3.1 Preparation of data

3.1.1 Common Mode

To subtract common modes, in a first iteration, the pedestal mean and width were found to define a threshold at 3σ above the pedestal mean for each pixel. Then the data were re-read, defining for each event those pixels with pulsheights below the 3σ cut as not-hit. In each event, the average deviation of the not-hit pixels from their respective pedestal means is subtracted from the pulseheights in all pixels. Figure 14 shows the common mode tube by tube for $1.3k$ events. As expected, the common mode behaviour is very similar for tubes on the same read-out board.

3.1.2 Cross Talk

In order identify cross talk, LED runs were used where the whole surface of the detector was illuminated reasonably uniformly, showing about 0.05 hits per pixel per event (after all corrections above a 5σ cut - see section 3.2) Four kinds of cross talk of different strength could be identified in the read-out electronics, as listed in table 15. Figure 16 shows the correlation coefficients between the pulseheights of the pixels with in the same tube, once read out with the fast read-out, once with the Camac system. The absence of cross talk in the Camac system confirms that the cross talk found is only in the read-out electronics, not in the tube itself. Similar plots to those in Figure 16, but showing the correlation coefficients for all channels on one read-out board (two tubes), were used to identify cross talk. In order to see a possible direction in the cross talk, i.e. cases where pixel y talks to pixel x, but x does not talk to y, also the probabilities were calculated, that a hit in pixel x is "caused" by a hit in pixel y, such as in figure 17. For the purpose of calculating this probability, a hit is defined as a pulseheight more than 5σ above the pedestal mean (as for photon counting), and it is assumed that the pixel with the larger pulseheight

Figure 16: Correlation coefficients between the pulse heights of pixels within one tube for Camac readout (left) and fast readout (right)

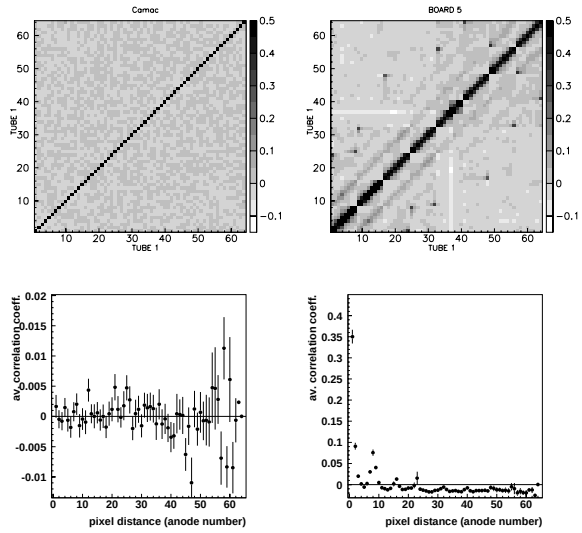

The value for the correlation coefficient across the diagonal is of course one. For better readability, the scale on the 2-D plots has been reduced to a maximum of 0.5.

Figure 17: Cross talk probabilities

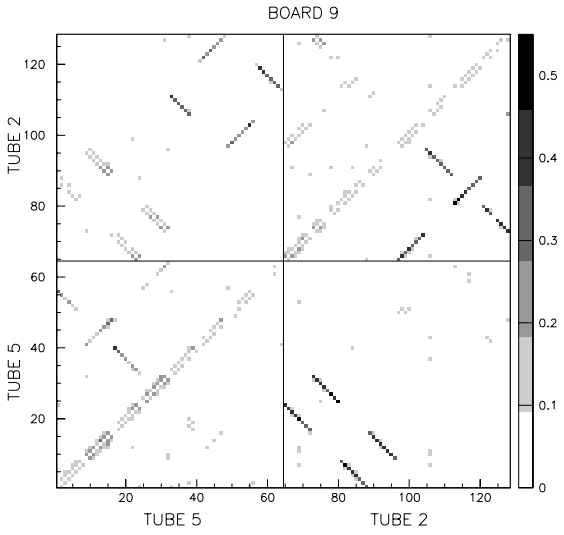

The plot entries are the probabilities that a hit in pixel x on the x-axis is "caused by" a hit in pixel y on the y-axis.

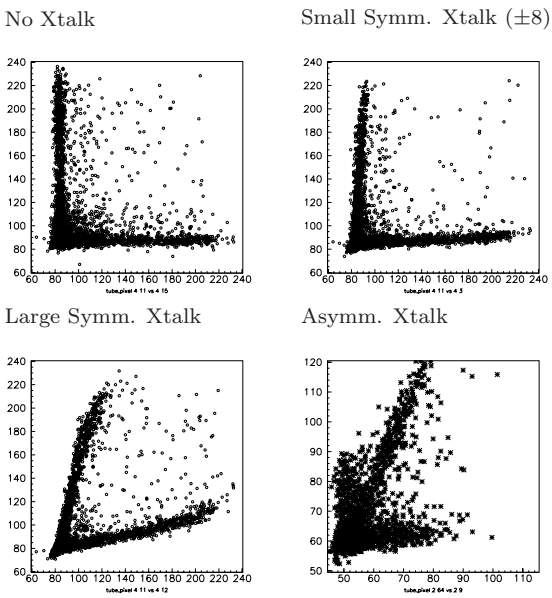

Figure 18: Scatter plots: pulse height in pixel x vs pulse height in pixel y for different pairs of pixels, showing either no, small symmetric, large symmetric or asymmetric cross talk.

"caused" the hit in the pixel with the lower pulse-height. Sometimes of course, there are two genuine hits (or hits induced by cross talk from other pixels) in a pixel pair, leading to a baseline-probability which is $\sim 5\%$ for the LED runs used. Figure 17 clearly shows symmetric as well as asymmetric cross talk. Examples of the correlation of the pulse-heights in cross-talk related pixel pairs are shown in figure 18. The asymmetric xtalk has some unusual properties. One is that there is no next-to-nearest neighbour cross talk, none of the charge induced by the pixel with apv sample number y to pixel $y-1$ is transferred further to pixel $y-2$. This is the reason that the scatter plot in figure 18 for the asymmetric cross talk looks as if the cross talk was sometimes "switched off" - the events without cross talk are those induced by asymmetric cross talk themselves. Another property of the asymmetric cross talk is, that it varies from board to board, and even inside the same board, but is very similar for groups of 32 with consecutive apv sample numbers.

3.2 Photon Counting

3.2.1 Principle

The basic photon counting procedure is to (pixel by pixel)

- histogram adc-spectra
- find pedestal mean (μ) and width (σ)
- define threshold cut (normally at $\mu + 5\sigma$
- count everything above the cut as one hit
- calculate the number of photo electrons from the number of hits

Finding the pedestal mean and width In order to find μ and σ, a Gaussian is fit to the pedestal, over a restricted range $[\mu - 8\sigma, \mu + 2\sigma]$, if $\sigma < 1$ $[\mu - 8\sigma, \mu + 2(\mathsf{adc\ counts})]$.

Electronics-Effects In the case of the fast readout electronics, the signal was corrected for common mode and cross talk, as described in the section on the 3×3 array.

Notation The following notation is used throughout the text N_{all} = number of events, $N_0, N_1, \ldots$ = number of zero, single, double, ... p.e. events in a given pixel, and $n_0 = \frac{N_0}{N_{\mathsf{all}}}, n_1 = \frac{N_1}{N_{\mathsf{all}}}, \ldots$, the fraction of zero, single, ... p.e. events. The fraction of events above a $m\sigma$ cut is $n_{m\sigma}$, e.g. $n_{5\sigma}$. For the fraction of single, double, ... p.e. events lost below the cut, the symbols $\epsilon_1, \epsilon_2, \ldots$ are used. The mean number of photo electrons per event in a given pixel denoted by $\lambda_{\mathsf{p.e.}}$.

The total number of p.e. $> 5\sigma$ When evaluating the performance of the tube, the total number of p.e. above the cut is of more interest than the total number of p.e. The number of photo electrons above the cut is:

$$\lambda_{m\sigma}^{\mathsf{true}} = \lambda_{\mathsf{p.e.}} - \epsilon_1 \lambda_{\mathsf{p.e.}} e^{-\lambda_{\mathsf{p.e.}}}$$

This quantity is less dependent on the geometry of the set-up than just the number of hits, which goes down as the probability of double hits goes up for example by moving the detector plane closer to the mirror. Still, while the number of p.e/evt is independent of the mirror-detector distance, the number of p.e./evt above the cut is not quite, because double p.e. events are less likely to be lost than single p.e. events. Therefore a yet more setup-independent number is the number of photo electrons above the cut, "as if they were all single p.e. events", i.e. in the limit of an infinite distance between detector and mirror:

$$\lambda_{m\sigma}^{\mathsf{all\ single}} = (1 - \epsilon_1)\, \lambda_{\mathsf{p.e.}}$$

The number that is actually calculated from the data, for each pixel, is:

$$\lambda_{m\sigma} = -\ln(1 - n_{m\sigma}) \tag{1}$$

This definition allows to estimate the above quantities without any knowledge of ϵ_1. As an estimate of $\lambda_{m\sigma}^{\mathsf{true}}$, $\lambda_{m\sigma}$ under-estimates $\lambda_{m\sigma}^{\mathsf{true}}$ by $\sim (1 - \frac{1}{2}\epsilon_1)\epsilon\lambda_{\mathsf{p.e.}}^2$, which is a relative error on $\lambda_{m\sigma}^{\mathsf{true}}$ of $< 3\%$ for the values of $\lambda_{\mathsf{p.e.}}$ and ϵ_1 considered here (5σ cut). As an estimate of $\lambda_{m\sigma}^{\mathsf{allsingle}}$, $\lambda_{m\sigma}$ over-estimates $\lambda_{m\sigma}^{\mathsf{allsingle}}$ by $\sim \frac{1}{2}(\epsilon_1 \lambda_{\mathsf{p.e.}})^2$ which correspond to a relative error of $< 0.5\%$ for the 5σ cut and the values of $\lambda_{\mathsf{p.e.}}$ and ϵ_1 found here.

Signal Loss ϵ_1 There are two sources of signal loss: the flow of photo electrons just stops at some stage in the dynode chain, due to the probability of e^{-g_i} that an electron arriving at dynode i with gain g_i produces 0 secondaries. This signal loss is dominated by the probability that a single p.e. arriving at the first dynode does not produce any secondaries, e^{-g_1}. The second source of signal loss is the loss due the pulse height being below the threshold cut.

To estimate the signal loss, the spectra are fit (pixel by pixel) with the function described in appendix A. The four parameters returned by the fit are the pedestal mean μ_p, pedestal width, σ, the number of p.e./event and the gain at the first dynode. From the shape of the single p.e. part of the function, and the gain at the first dynode, both types of signal loss can be estimated.

3.2.2 3×3 array of MaPMTs

The basic procedure The common-mode corrected spectra are used to find pedestal mean and sigma as described in the beginning of this section. The greatest problem for photon counting in the 3×3array is the presence of cross talk that needs to be corrected for.

Removing Cross Talk Two different techniques are used to correct for cross talk. **Method a** is based on rejecting, event bey event, each hit in a pixel, if one of the cross-talk partners of that pixel has a hit with a higher pulseheight. Losses due to genuine double hits are recovered at the end of the procedure, using statistics to calculate the probability for each pixel to loose a hit due to a genuine hit in one of its cross talk partners. To calculate this probablility, it is assumed that in the case of genuine double hits, the probability $p(h_x > h_y)$, that the pulseheight in y, h_y, is larger than the pulseheight its cross-talk partner x, h_x, is $\frac{1}{2}$. The uncertainty in the photon counts due to this assumption is estimated to be less than 1% for the Čerenkov ring data.

In **Method b**, the pulse height in each individual pixel in each event is corrected. For each event, for each pixel x, a fraction f_{xy_i} of the pulse height in each of the pixels y_i that talk to x is subtracted from the pulse height in x. This fraction is determined from plots of the ratios of pulseheights in cross talk related pixels, obtained from an LED run, such as in figure 19. The additional peak at ~ 0 in figure 19 b) is due to the property of the asymmetric cross talk that none of the charge passed from apv-sample number y to $y-1$ is passed on to $y-2$, i.e. the events in that peak are induced by asymmetric cross-talk themselves; the algorithms that corrects the pulseheights is able to pick out such events.

The two methods agree up to $\sim 7\%$ (figure 22). The largest difference (20%) is in tube 4, where the event by event cross-talk correction was not completely successful. It is the tube with the largest gain and the largest cross talk contribution; because the ratio of the average pulse height to the pedestal width (which defines the cut) is much higher for this tube than for any of the others, it is much more sensitive to small errors in the estimated cross talk ratio. Figure 20 shows a pulseheight spectrum before and after the event-by-event cross talk correction is applied.

Fits to spectra, Signal Loss In order to establish the signal loss, the spectra are fit with with a function as described in the section 3.2.1. Only Čerenkov data are used, as LED data suffer far more from cross talk and imperfect cross talk correction. As a sufficient number of hits is needed to determine the signal shape, only spectra from pixels with at least 0.05 p.e./evt are selected. As these are the ones contributing most to the photon counts, they are also the most relevant ones. Only those spectra are accepted where the χ^2 per degree of freedom is less than 3. Figure 21 shows an example of a fitted spectrum, with the single p.e.

Figure 19: Pulse height ratios $\frac{\text{[pulsheight talked-to]}}{\text{[pulseheight talking]}}$

a) symmetric xtalk b) asymmetric xtalk

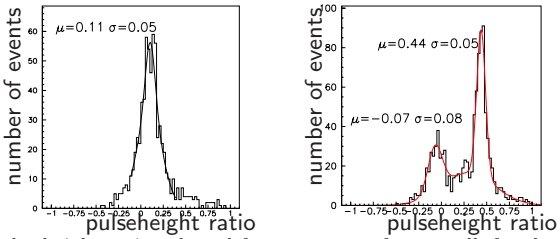

pulse-height ratios plotted for two types of cross talk for the same talking pixel in tube 2. (Only for [pulse-height talking] is a hit, i.e. 5σ above the pedestal mean.). The spectra are fit with a Gaussian for each peak plus one (wide) Gaussian for genuine double hits (i.e. 2 Gaussians for a), 3 for b)).

Figure 20: Spectra before and after correction

Before correction After correction

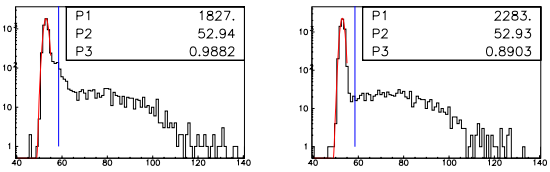

Figure 21: Example of a fit to pulse height spectra of pixels after event by event cross talk correction. Solid, fat line: total fit, dashed: single photo electrons

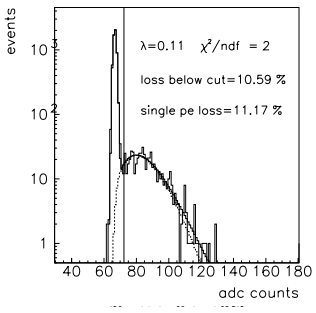

tube 2 pix 28
gain: 4.1
loss below cut: 11%
total single pe loss: 12.6%

Table 2: Signal loss estimates

these results will be up-dated

	from run with lenses				from run without lenses				
Tube	number of pixels	Loss below cut	Gain 1st dyn	total loss	Tube	number of pixels	Loss below cut	Gain 1st dyn	total loss
1	3	$(4.5 \pm 1)\%$	3.0 ± 0.2	$(9.4 \pm 2)\%$	1	3	$(6.3 \pm 2)\%$	2.8 ± 0.2	$(13 \pm 5)\%$
2	9	$(10 \pm 4)\%$	3.6 ± 0.6	$(13 \pm 6)\%$	2	8	$(11 \pm 4)\%$	3.5 ± 0.5	$(14 \pm 6)\%$
3	4	$(13 \pm 2)\%$	2.5 ± 0.2	$(20 \pm 3)\%$	3	0			
4	0				4	2			
5	0				5	0			
6	7	$(5.0 \pm 2)\%$	3.6 ± 0.3	$(7.9 \pm 3)\%$	6	9	$(6.1 \pm 2)\%$	3.8 ± 0.3	$(8.4 \pm 2)\%$
7	2	$(4.0 \pm 2)\%$	4.3 ± 0.4	$(5.5 \pm 2)\%$	7	2	$(5.5 \pm 0)\%$	3.8 ± 0.4	$(7.9 \pm 1)\%$
8	9	$(8.6 \pm 3)\%$	3.1 ± 0.5	$(14 \pm 5)\%$	8	9	$(9.3 \pm 4)\%$	3.2 ± 0.6	$(14 \pm 7)\%$
9	2	$(5.0 \pm 2)\%$	5.2 ± 0.3	$(6 \pm 2)\%$	9	0			

(The two pixels from tube 9 have a higher χ^2)

part of the fit function superimposed as a dotted line. From the shape of the fit-function, the loss of single p.e. events below the cut and the signal loss at the first dynode can be calculated. The results (table 2) are averaged over each tube and applied to the Monte Carlo simulation.

Dead Pixels A few channels are dead. Lab-tests showed that this is not due to a fault in the MaPMTs themselves, which is also confirmed by the fact that the dead channels still cross-talk to their neighbours. An LED run was used to identify dead channels and channels getting a very large number of hits after the cross talk correction; these channels are ignored in both, the data and the MC photon count. Altogether 36 channels were masked, most of them in tubes 7 and 9 (24 channels); only 4, 6 masked channels correspond to pixels on the Čerenkov ring with and without lenses respectively.

Background Background is estimated assuming a flat background and averaging, tube by tube, over all pixels that were clearly not on the Čerenkov ring.

Photon Counts, Data & MC The numbers given in figure 22 are $\lambda_{5\sigma}$, i.e. the p.e. counts above 5σ, corrected for multiple p.e. events and cross-talk corrected using Method a (statistical). The signal loss results are applied to the Monte Carlo results. The same set of pixels is masked in data and MC.

Errors ($\lambda_{5\sigma}$) Given the large number of events (6000 per run), statistical errors are negligible. Systematic errors have been estimated by comparing the two different cross talk correction methods, (excluding tube 4 where the pulseheight correction method clearly failed). This contributes 4.5%. The error due to the assumption of $p(h_x > h_y) = \frac{1}{2}$ is estimated by trying different values and found to be $\sim 1\%$. Comparing the photon counts for the same set-ups but different runs (figure 23) gives an error estimate of $\sim 1.2\%$. Adding all these error

Figure 23: Comparing Results ($\lambda_{5\sigma}$)

With lenses

	run 2634			run 2662		
signal	0.59	1.09	0.66	0.57	1.06	0.65
	1.00	0.00	1.13	1.01	0.00	1.09
	0.60	0.83	0.61	0.63	0.79	0.64
	total sg 6.52			total sg 6.44		

Without lenses

	run 2631			run 2610		
signal	0.39	0.83	0.37	0.39	0.80	0.37
	0.85	0.00	0.92	0.86	0.00	0.93
	0.20	0.66	0.26	0.20	0.64	0.30
	total sg 4.48			total sg 4.49		

contributions in quadrature gives an estimate for

MC numbers are not the final

Figure 22: Photon Counting Results (p.e./evt after a 5σ cut, corresponding to $\lambda_{5\sigma}$in eq 1), data display integrated over 6k events

	No correction	With lenses method b	method a)	without lenses method a)
data display	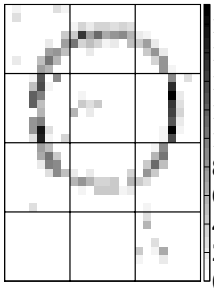	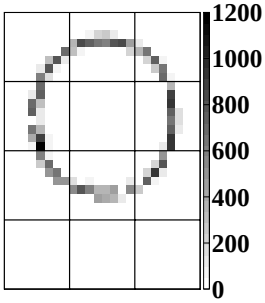	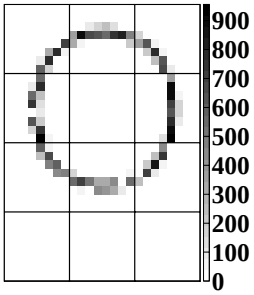	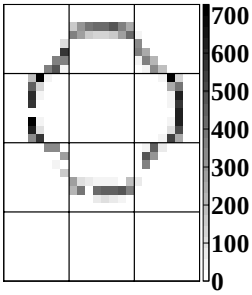
sg+bg	1.43 2.12 0.95 2.73 0.42 2.34 1.30 1.09 1.23 total sg+bg 13.61	0.65 1.14 0.68 1.25 0.03 1.19 0.68 0.93 0.70 total sg+bg 7.25	0.62 1.12 0.68 1.04 0.02 1.16 0.63 0.86 0.65 total sg+bg 6.78	0.41 0.82 0.39 0.88 0.01 0.96 0.21 0.66 0.35 total sg+bg 4.69
backg.		0.03 0.03 0.03 0.05 0.03 0.03 0.03 0.02 0.05 total bg 0.29	0.03 0.03 0.03 0.03 0.02 0.03 0.03 0.02 0.03 total bg 0.26	0.02 0.02 0.02 0.02 0.01 0.03 0.01 0.03 0.05 total bg 0.21
signal		0.62 1.11 0.65 1.20 0.00 1.16 0.66 0.90 0.66 total sg 6.96	0.59 1.09 0.66 1.00 0.00 1.13 0.60 0.83 0.61 total sg 6.51	0.39 0.80 0.37 0.86 0.00 0.93 0.20 0.64 0.30 total sg 4.49
MC			0.61 1.04 0.54 0.99 0.00 1.06 0.49 1.04 0.44 total MC 6.21	0.30 0.80 0.26 0.70 0.00 0.78 0.27 0.68 0.15 total MC 3.94

the systematic error in $\lambda_{5\sigma}$ for the whole ring of 5%.

3.2.3 Varying the Angle of Incidence

The performance of the array with lenses was tested for the case where the photons do not arrive at normal incidence, but at an angle α relative to the normal on the detector plane. LED runs were used for these tests. Tilting the array by an angle α will lead

Figure 24: Loosing and re-gaining photons in a tilted lens array by shifting the lenses relative to the MaPMTs.

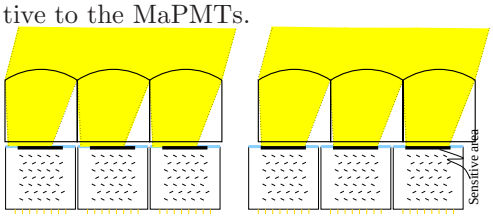

to loss due increased reflection losses, a reduction in effective area area $\propto \cos(\alpha)$ and due to a shift in the image produced by the lens array on the MaPMT cathode. As long as the image is not outside the lens (which has non-transparent sides), the loss due to the shift can be completely recovered by shifting the lens array relative to the MaPMTs, to bring the sensitive area of the photo cathode back underneath the image from the lenses, as illustrated in figure 24. Figure 25 shows the results in terms of the average number of hits per pixel (ignoring dead pixels) depending on the column the pixel is in. The column ordering is such that column 1 corresponds to the left in figure 24, column 8 to the right. Some of the lenses had blackened sides, while others have diffuse, transparent sides, seperated with white paper. Those lenses with transparent sides at the left or right edge of the array are ignored in the analysis. Tabel 3 shows the results for the "ideal shift" measurements sperately for lenses with black sides and lenses with diffuse sides and compares them with the expectation from the 0^o case, considering all the contributions to the loss of photons mentioned above. For the 20^o case, the loss is dominated by the reduction in effective area (area $\propto \cos\alpha$), while for the 30^o case, a significant fraction of the lens image is outside the lens. The disagreement between expected and measured values for 30^o, diffuse sides, is interpreted as some of

Table 3: hits/evt/tube

	0^o	20^o		30^o	
	get	expect	get	expect	get
black	4.05	3.68	3.55	2.93	2.98
diffuse	3.64	3.31	3.42	2.64	2.98

'expect' is the number of p.e. expected given the value for 0^o and the known sources of signal loss due to the tilt, assuming that light that hits the side of the lens (only relevant for 30^o) is lost, which is not quite true for the diffuse sides, hence the disagreement for the 30^o case.

Figure 26: Single MaPMTs, using an Air radiator at 49mbar, with/without lenses

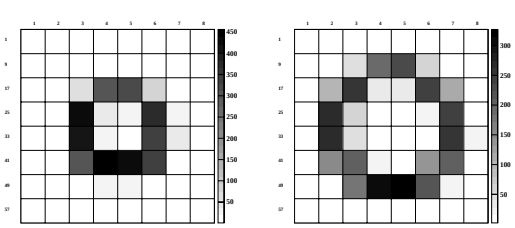

the light hitting the side of the lens (that is treated as lost when calculating the expected value) being reflected back onto the cathode surface.

3.2.4 Single MaPMT

In a first test beam in May, single MaPMTs, read out with the Camac system, were tested in order to evaluate the performance of the new batch of MaPMTs and, for the first time, their performance with the lenses. Air was used as a radiator, at atmospheric pressure (n-1=??), producing ring-segments on the tube's surface, and at very low pressure (49mbar, n-1=??), such that a whole Čerenkov ring from a 120GeV pion with a mirror of 1m focal length would fit on a single tube (fig 26) The MaPMTs were read out with the Camac system [reference]. Several configurations were tested: With and without lenses, with and without a pyrex filter in front of the tube and with/without the quartz window that separates the radiator gas from the photo detectors. The results (table 4) show that the performance of the lenses agrees very well with expectation.

Figure 25: Av. number of hits/pixel depending on left-right position for light coming from the right (column 8) at different angles

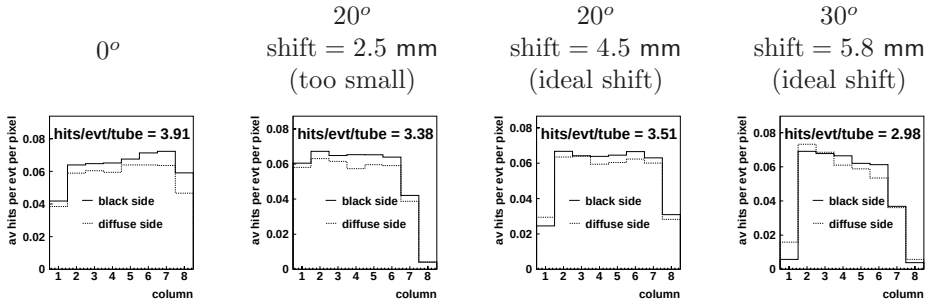

Table 4: Single PMT Photon Counts ($\lambda_{5\sigma}$)

Full ring, (49mbar) tube 1		
	With lens	without lens
Backg.	0.022	0.014
Signal	0.259	0.274
Ratio without/with: 1.06 (expect: 1.09)		

Full ring (49mbar), tube 2		
	With pyrex filter	Without pyrex filter
Backg.	0.016	0.016
Signal	0.16	0.26
Ratio with/without: 0.62		

Ring segment (athm pressure), tube 1			
	with lens, with window	no lens, with window	no lens, no window
Backg.	0.024	0.027	0.056
Signal	1.00	0.75	0.82
ratio	1.33	1	1.08
expect	1.31	1	1.09

Signal corresponds to $\lambda_{5\sigma}$ as defined in eq 1, after background subtraction. The background is estimated by averaging over pixels that are clearly outside the ring.

4 LED scan results

4.1 Single channel response

The response of the multianode photomultiplier tubes to single photons has been measured with the scanning facility described in Section 2.6 The photocathode of the MaPMT was operated at a voltage of -900 V. The LED intensity was set such that for about 30 % of the events at least one photon electron is produced at the photocathode within the timing gate of 200 ns. The DAQ recorded events with a trigger rate of about 1000 Hz. In Figure 27 we show a measured pulse height spectrum. The broad signal containing mostly one photo electron and the pedestal peak are clearly visible. The mean pulse height is at around 100 ADC counts above pedestals. The spectrum has been fitted by a function which allows a Gaussian shape for each photo electron signal and for the pedestal peak. The number of photo electrons n_{pe} in an event has to follow a Poisson distribution. The variances of the Gaussian signal shapes are constrained to be proportional to $\sqrt{n_{pe}}$. The fit is superimposed on the data points. The variance of the single photon signal is about 50 ADC counts. Comparing the width of the single photon peak with its mean value yields a lower limit of 3.7 for the gain at the first dynode. This corresponds to a probability of 2.5% or less for no multiplication occurring at the first dynode. The signal to pedestal width ratio is 40:1.

We have also studied the dependence of the gain of the MaPMT on different parameters. The gain becomes larger with increasing negative high voltage applied to the photocathode. In Figure 28 we

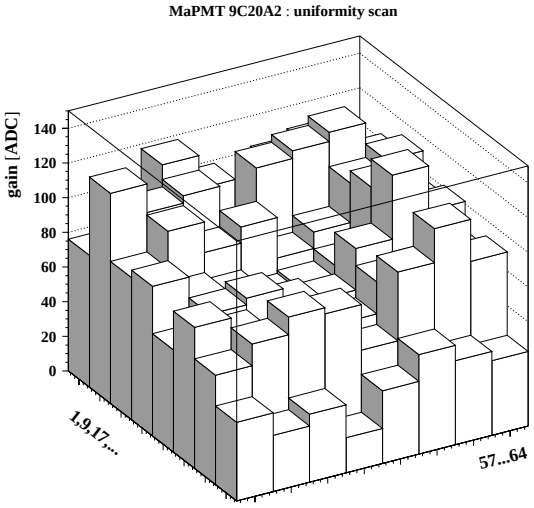

Figure 29: Mean pulse height of all 64 channels of an MaPMT.

plot the measurements of the mean pulse height above pedestal and the variance of the single photon signal versus the high voltage applied at the photo cathode. The gain varies for the 64 different dynode chains within a tube. In Figure 29 we show the mean pulse height of all 64 channels of one tube. The gain variations are about a factor of two with an RMS spread of about 30 % about the mean value. A degradation of the gain is visible for the edge columns. This has been investigated in more detail by scanning across the tubes in steps of 0.1 mm. The measured gain as a function of the position of the light source across the tube is shown in the top of Figure 30. For the edge pixel the gain of is clearly inhomogenous and drops before the geometrical edge of the pixel. This is also reflected in the measurement of the average number of observed photons, λ, as shown in the bottom of Figure 30. The collection efficiency which is proportional to λ deteriorates towards the edge of the pixel. This reduces the overall efficiency of the MAPMT by a few percent. The pixel size as defined by the 50% efficiency points of a pixel is 2.1 mm which is a little larger than the 2.0 mm opening of the dynodes reported from the manufacturer.

Table 5: Pulseheight ratio talking/talked-to (Camac read-out with LeCroy amplifier)

channels	1 vs 2	2 vs 1	3 vs 2	2 vs 3
xtalk ratio	0.34%	0.30%	0.73%	0.65%
channels	5 vs 2	6 vs 2	7 vs 2	8 vs 2
xtalk ratio	0.77%	0.48%	0.77%	0.64%

4.1.1 Cross talk

Lab tests using the Edinburgh scanning facility were used to identify possible cross talk within the tube. Several pixel pairs have been investigated, using two different Camac setups (one with a LeCroy amplifier, one with a Philips amplifier). The tests confirm that none of the cross talk seen in the testbeam is in the tube (fig 31). The tests show some very small residual cross talk the origin of which has not been identified, but the fact that it is seen to the same extent in neighbouring pixels as in pixels two or three channels apart strongly suggests it is in the electronics (table 5). The fraction of charge deposited by this cross talk is typically 0.5%, and always less than 1%.

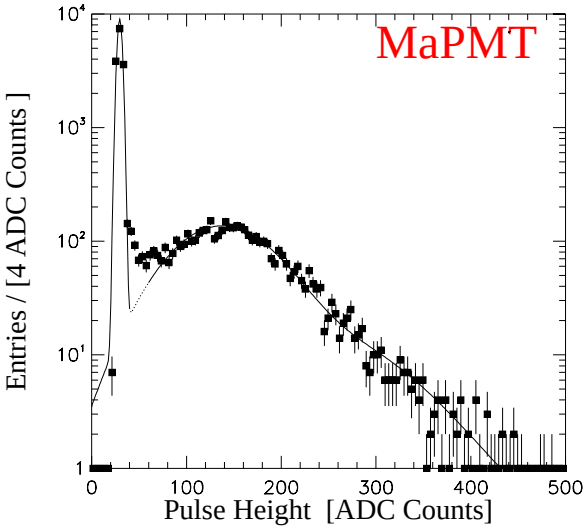

Figure 27: Single photon spectrum of MaPMT pixel.

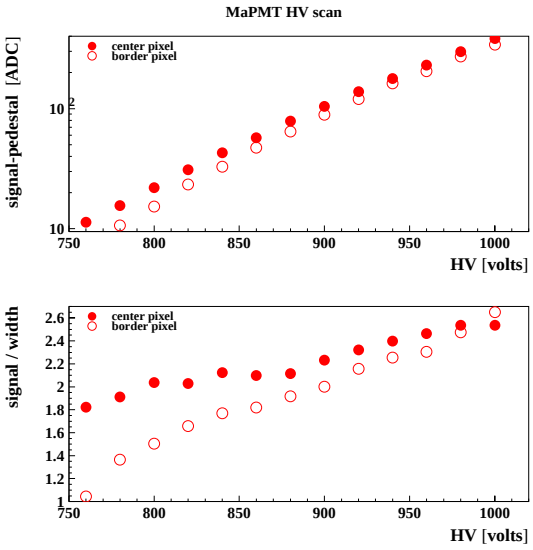

Figure 28: High voltage scan. Top plot is gain and bottom plot is width versus high voltage.

Table 6: Common modes in lab tests (Gaussian fit)

	attached to MaPMT	just electronics
mean	52.6	52.3
σ	1.54	1.48

4.2 Signal loss

Signal loss studies to follow....using Jonas fit

4.3 Studies of the pipelined electronics

4.3.1 Common mode corrections

The common mode of the signal was calculated as described in Section 3.1.1. The widths and means of the common mode distributions of from channels that were attached to the MaPMT and from those that were not are in agreement (table 6), which corroborates the assumption that the common mode fluctuations are related to the ASIC and not the tubes themselves. The larger width observed in the lab tests can be attributated to the differing power supplies used and the differing noise environments between the LED scanning facilities and the test beam.

4.3.2 Cross talk

The forms of cross talk observed in the test beam analysis have been studied in the LED scanning facility. In Figure 4.3.2 the ADC counts for two pixels corresponding to the relationships in which cross talk was observed as described in Section 2.4. *(note: currently integrated over several pixels will produce a cleaner plot before next draft)*

4.4 Recovery time

5 Charged particle studies

Our assumption: that all lens dimensions, window thicknesses etc have been given already. window 8mm, lens 24 mm thick with radius of curvature 25 mm

NB we are still looking at issue of multi-hit pixels. At present all is binary. Will decide what to do and

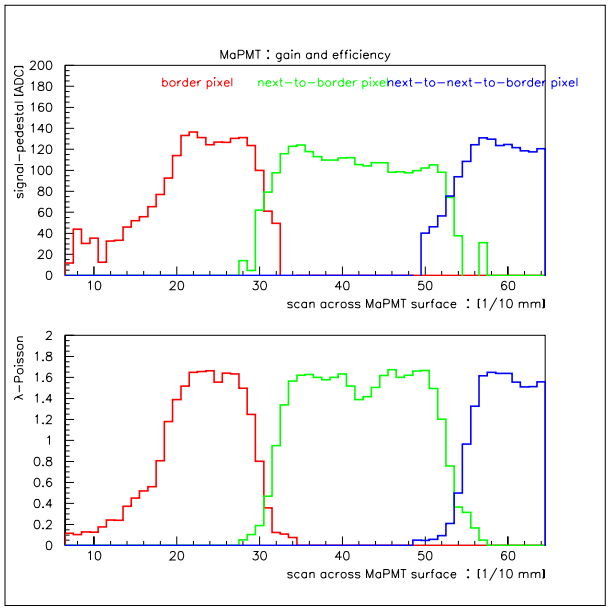

Figure 30: Scan across an MaPMT.

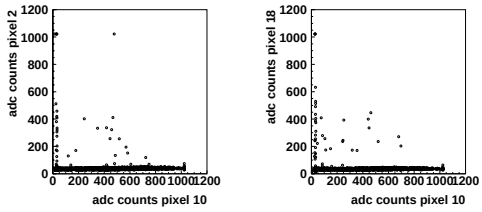

Figure 31: Scatter plots of pulse heights of neighbouring pixels, obtained with the Edinburgh LED scanning facility. The light spot was directed onto pixel 10 (reading out channels $2, 10, 18, \ldots, 58$)

Cross talk

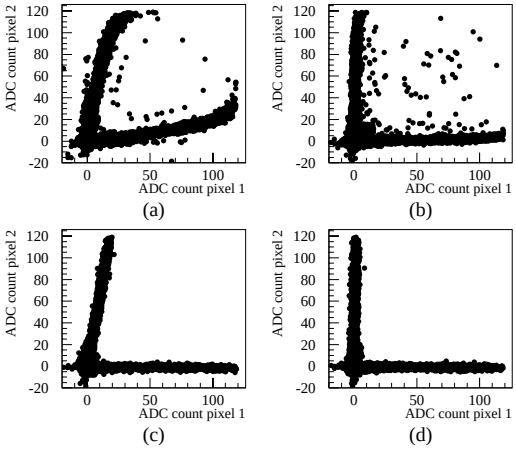

Figure 32: The ADC counts for two pixels that followed the relationships: (a) adjacent AC-coupler channels, (b) pixel numbers ± 8, (c) next APVm sample and (d) no observed cross talk. The board used was 9.

be more explicit in the text when this is clear to us.

A single MAPMT was placed on a rotaing platform in the beam line, and data were taken with 120 GeV/c pions traversing the MAPMT with and without a quartz lens. A variety of angles were scanned in the horizontal plane ranging from 0 degrees, corresponding to charged particles impinging on the MAPMT window (or lens), to 180 degrees, corresponding to charged particles impinging on the back of the MAPMT. The particle impact point and tracjectory is defined by a two silicon telescope planes 421 cm and 30 cm in front of the tube, and one plane 427 cm behind it. For this analysis only triggers with single hits per plane were considered. The setup and definition of angle is indicated in figure 5.

The configuration was modelled in a dedicated simulation which included a full description of the MAPMT lens, window and gap between the two, together with the transmission, reflection and absorption probabilities at these boundaries. *(more detail intended for the second draft!)*

Data taken without lens

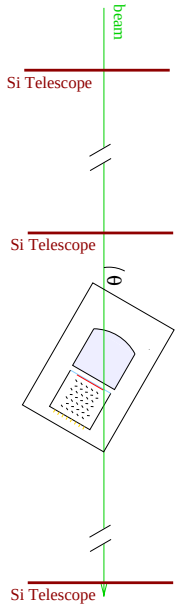

Figure 33: A schematic of the set up showing angle definition, centre of rotation etc

Figure 34: Data and simulation for no lens case.

Figure 5 shows the mean number of MAPMT pixel hits per charged particle, as a function of the horizontal impact point of the charged particle on the MAPMT window, for different angles. In the vertical coordinate, the charged particle trajectory was limited to a band of ±6.5 mm (5 Si-pixel) around the centre of the lens. It can be seen that a mean number of 3 to 5 pixels per event were hit, depending on the incoming particle angle. This number increased up to 24 when the MAPMT was placed perpendicular to the beam and the particle traversed the whole window. These results are in agreement with those from simulation, which are also indicated on figure 5 (*I hope so – I have to run it for this configuration!*).

Data taken with lens

With the addition of the quartz lens in front of the MAPMT there is a significantly enhanced radiator length. However there was no optical coupling made between the lens and the window, and consequently many of the photons produced in the lens undergo internal reflection at this boundary. Nevertheless, there is an increased yield in detected photoelectrons, which on average is spread more widely over the MAPMT pixels. Figure 5 shows the mean number of MAPMT pixel hit per charged particle, with the same conventions as in figure 5. For small incoming particle angles, 7 to 9 pixels were hit. At angles around 45 degrees (from 30 to 60) 20 to 30 pixels were hit. It can be seen that both the absolute number of hits, and the angular and position dependencies, are well described by the simulation.

need to discuss somewhere about the blacking of the walls of the lens

6 Magnetic Field Studies

The MAPMTs must be able to cope with the magnetic fringe fields of the LHCb dipole magnet. Even with a large shielding plate upstream of the magnet[2] the strength of these fringe fields will not be negligible. In the photodetector plane of RICH 1 we expect magnetic fields of up to 30 Gauss, mainly in the vertical direction. The photodetector plane of RICH 2 will be protected by an additional shielding cage and the expected fringe fields are similar.

The sensitivity of the MAPMT to magnetic fields has been studied by placing a single tube into a Helmholtz coil which can provide axial magnetic fields of up to 30 G. Using a LED light source, the efficiency of the tubes has been measured for magnetic fields transverse, (B_x and B_y) and parallel (B_z) to the photodetector axis [10]. In Figure 36 a) we show the measured number of photoelectrons versus the strength of the magnetic field for these three configuration. This demonstrates that the MAPMTs are quite insensitive to transverse magnetic fields up to 30 G. For longitudinal fields of $B_z \geq 10$ G, however, the efficiency of the MAPMT deteriorates. This loss occurs mostly in the two edge rows, parallel to the x-axis *CHECK this, could be better with new tubes* where the focusing of the photo electrons onto the first dynode is most sensitive to magnetic fields. At $B_z = 30$ G the collection efficiency of the edge rows is reduced to 50 % with respect to $B_z = 0$ G. The effect of shielding the MAPMT with a $\mu-$metal tube of wall thickness 0.9 mm has been measured. In

[10] The photo detector axis is defined as the normal direction to the photocathode.

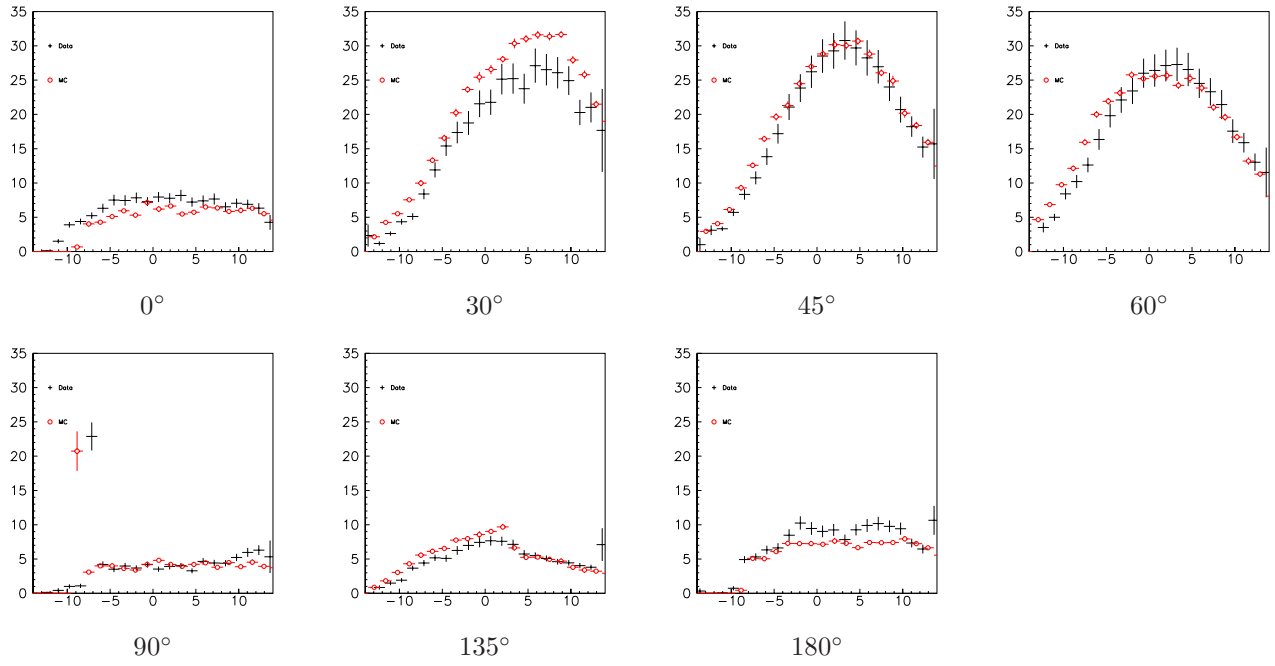

Figure 35: Data and simulation for no lens case.

Figure 36 b) we plot the measured number of photoelectrons versus B_z without and with the shielding tube extending out with the MAPMT window face along the z-axis by 13 mm and 32 mm, respectively. The $\mu-$metal tube effectively reduces the efficiency loss. At 32 mm extension efficiency is not affected by the magnetic field anymore. Additional measurements have been carried out with a pin-hole mask put in front of the MAPMT window to better define the aperture of the individual pixels; the effect of the magnetic fields on selected pixels has also been looked at. The studies corroborates the conclusion that the MAPMT can be effectively shielded with a $\mu-$metal structure. An estimate of the field strength required to saturate this $\mu-$metal is around 300 G.

7 Summary and conclusions

References

[1] T. Gys *et. al.*. *Paper for 1999 test beam.*

[2] The LHCb Collaboration. *LHCb Technical Proposal. CERN/LHCC/98-4, (1998).*

[3] E. Albrecht *et. al.*. *Submitted to Nucl. Instr. and Meth, hep-ex/0001053.*

[4] MDM de Fez-Lazo *et. al.*. *Nucl. Instr. and Meth* **A382** *(1996) 533.*

[5] M. Raymond *et. al.*. *London 1997, Electronics for LHC Experiments, CERN/LHCC/97-60, (1997) 158.*

[6] L.L. Jones *et. al.*. *Rome 1998, Electronics for LHC Experiments, CERN/LHCC/98-36, (1998) 185.*

[7] Philips Semiconductors. The I^{2}C-Bus Specification, Version 2.1, January 2000. *http://www.semiconductors.com/acrobat/various/I2C_BUS_SPECIFICATION_3.pdf.*

[8] The CMS Collaboration. *The Tracker System Project Technical Design Report. CERN/LHCC/98-6 (1998).*

[9] M. Raymond *et. al.*. *Nucl. Instr. and Meth* **A351** *(1994) 449.*

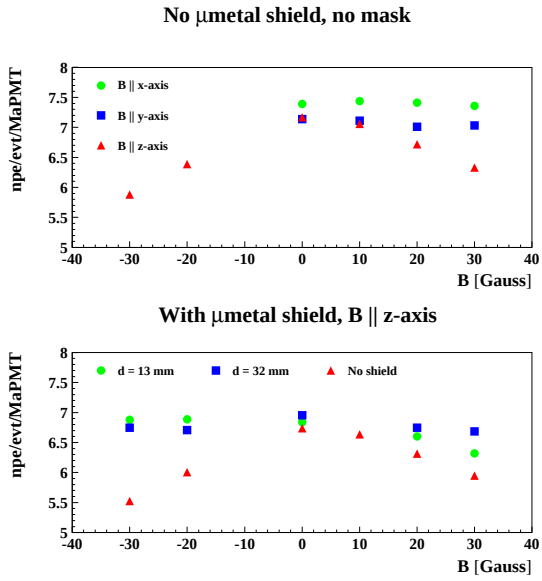

Figure 36: The number of observed photoelectrons from an LED source is plotted versus the magnetic field strength for (a) perpendicular, B_x and B_y, and longitudinal, B_z, fields. In (b) the effect of shielding the MAPMT with a $\mu-$metal tube is shown.

[10] J. Christiansen. *LHCb 99-029 ELEC.*

[11] N. van Bakel *et. al.. Snowmass 1999, Electronics for LHC Experiments, CERN/LHCC/98-33, (1999) 167.*

[12] F. Anghinolfi *et. al.. IEEE Trans. Nucl. Sci.* **44** *(1997) 298.*

[13] Rutherford Appelton Laboratory M. Morrisey. *SEQSI Manual, Unpublished.*

[14] S.A. Baird *et. al.. Snowmass 1999, Electronics for LHC Experiments, CERN/LHCC/98-33, (1999) 357.*

[15] Rutherford Appelton Laboratory J. Coughlan. *CMS Front-End Driver PMC, User Manual, Unpublished.*

[16] E. Albrecht *et. al.. Nucl. Instr. and Meth* **A411** *(1998) 249.*

[17] O. Toker *et. al.. Nucl. Instr and Method A* **340 (1994) 572**.

[18] E. Albrecht *et. al.. Submitted to Nucl. Instr. and Meth in January 2000.*

[19] R. Abjean *et. al.. Nucl. Instr and Method A* **292 (1990) 593**.

A Fitting Spectra

A.1 Deriving an expression for the number of photo electrons arriving at the end of a dynode chain

Assuming the number of photo electrons coming from the cathode follows a Poisson distribution with mean λ_1, the probability to find k_1 photo electrons *arriving* at the first dynode is:

$$P(k_1) = e^{-\lambda_1}\frac{\lambda^{k_1}}{k_1!} \tag{2}$$

For each of the electrons arriving at the first dynode the dynode returns 0 or 1 or 2 or ... electrons, according to a Poisson distribution with a mean of $\lambda_2 = g_1$, where g_1 is the gain at the first dynode.

So the probability to find k_2 electrons after the first dynode is:

$$P(k_2) = \sum_{k_1=0}^{\infty} P(k_1) \sum_{n_1+\ldots+n_{k_1}=k_2} \prod_{i=1}^{k_1} e^{-\lambda_2}\frac{\lambda_2^{n_i}}{n_i!} \tag{3}$$

using the polynomial formula:

$$(a_1+\ldots+a_r)^m = \sum_{n_1+\ldots+n_r=m} \binom{m}{n_1,\ldots,n_r} a_1^{n_1}\ldots a_r^{n_r}$$

where

$$\binom{m}{n_1,n_2,\ldots,n_r} \equiv \frac{m!}{n_1!n_2!\ldots n_r!}, \quad \sum_{i=1}^{r} n_i = m$$

and choosing $m = k_2$, $r = k_1$ and $a_i = 1$, one gets

$$\sum_{\sum n_i = k_2} \frac{1}{\prod_{i=1}^{k_1} n_i!} = \frac{k_1^{k_2}}{k_2!} \tag{4}$$

and hence:

$$P(k_2) = e^{-\lambda_1}\frac{\lambda_2^{k_2}}{k_2!}\sum_{k_1=0}^{\infty}\frac{(\lambda_1 e^{-\lambda_2})^{k_1}}{k_1!}k_1^{k_2} \tag{5}$$

Generalising this for $n-1$ dynodes:

$$\begin{aligned} P(k_n) &= e^{-\lambda_1}\frac{\lambda_n^{k_n}}{k_n!} \\ &\sum_{k_1=0}^{\infty}\sum_{k_2=0}^{\infty}\cdots\sum_{k_{n-1}=0}^{\infty} \\ &\frac{(\lambda_1 e^{-\lambda_2})^{k_1}}{k_1!}\frac{(\lambda_2 e^{-\lambda_3}k_1)^{k_2}}{k_2!} \\ &\frac{(\lambda_3 e^{-\lambda_3}k_2)^{k_3}}{k_3!}\cdots \\ &\frac{(\lambda_{n-2}e^{-\lambda_{n-1}}k_{n-3})^{k_{n-2}}}{k_{n-2}!} \\ &\frac{(\lambda_{n-1}e^{-\lambda_n}k_{n-2})^{k_{n-1}}}{k_{n-1}!}k_{n-1}^{k_n} \end{aligned} \quad (6)$$

This looks already like a series of exponentials, if there weren't the last term with the summation parameter k_{n-1}, which is the only one that does not appear in the form $\frac{x^k}{k!}$, but instead $\frac{x^k}{k!}k^{k_n}$ Using

$$k_{n-1}^{k_n} = \frac{\mathsf{d}^{k_n}}{\mathsf{d}y^{k_n}}e^{yk_{n-1}}\Big|_{y=0} \quad (7)$$

we can write this last term as

$$\begin{aligned} &\frac{(\lambda_{n-1}e^{-\lambda_n}k_{n-2})^{k_{n-1}}}{k_{n-1}!}k_{n-1}^{k_n} \\ =\ &\frac{\mathsf{d}^{k_n}}{\mathsf{d}y^{k_n}}\frac{(\lambda_{n-1}e^{-\lambda_n}k_{n-2}e^{y})^{k_{n-1}}}{k_{n-1}!}\Big|_{y=0} \end{aligned} \quad (8)$$

which allows us to perform subsequently all the summations up to ∞, getting exponentials of exponentials of...

Starting off with an average of λ_1 photo electrons arriving at the first dynode, after $n-1$ dynodes with the gains $\lambda_2, ...\lambda_n$, the probability to find k_n electrons is:

$$\begin{aligned} P(k_n) &= e^{-\lambda_1}\frac{\lambda_n^{k_n}}{k_n!}\frac{\mathsf{d}^{k_n}}{\mathsf{d}y^{k_n}} \\ &\exp(x_1\exp(x_2\exp(x_3\cdots \\ &\exp(x_n\exp(y))\cdots)))\Big|_{y=0} \end{aligned} \quad (9)$$

$$\text{with } x_i := \lambda_i e^{-\lambda_{i+1}}$$

A.2 Calculating $\frac{\mathsf{d}^{k_n}}{\mathsf{d}y^{k_n}}e^{x_1e^{x_2\cdots e^{x_ne^y}}}\Big|_{y=0}$

In order to calculate $P(k_n)$ it is useful to make the following definitions:

$$\begin{aligned} f_0 &= e^{x_1e^{x_2\cdots e^{x_ne^y}}} \\ f_1 &= e^{x_2e^{x_3\cdots e^{x_ne^y}}} \\ f_2 &= e^{x_3e^{x_4\cdots e^{x_ne^y}}} \\ &\vdots \\ f_{n-1} &= e^{x_ne^y} \\ f_n &= e^y \end{aligned} \quad (10)$$

Then

$$\begin{aligned} f_0' &= f_0x_1 & f_1x_2 & \cdots & f_{n-1}x_n & f_n \\ f_1' &= & f_1x_2 & \cdots & f_{n-1}x_n & f_n \\ f_2' &= & & \cdots & f_{n-1}x_n & f_n \\ &\vdots & & & & \\ f_n' &= & & & & f_n \end{aligned} \quad (11)$$

Which gives a recursive formula for the first derivative:

$$\begin{aligned} f_i' &= f_ix_nf_{i+1}' \ i<n \\ f_n' &= f_n \end{aligned} \quad (12)$$

From which we get a recursive formula for the $m+1st$ derivative:

$$f_i^{(m+1)} = \sum_{k=0}^{m}\binom{m}{k}f_i^{(m-k)}x_{i+1}f_{i+1}^{(k+1)} \quad (13)$$

$$\text{with } f_n^{(k)} = f_n \ \ \forall k\in\mathbb{N}$$

which finally allows to calculate

$$P(k_n) = e^{-\lambda_1}\frac{\lambda_n^{k_n}}{k_n!}f_0^{(k_n)}(y)\Big|_{y=0}$$

by starting with $f_n(0)=1$ and calculating $f_i^{(m)}$ subsequently for all values $i=n,n-1,\ldots,0$ and all values $m=0,1,\ldots,k_n$.

A.3 Numerical Problems

The factor $\frac{\lambda_n^{k_n}}{k_n!}$ For any reasonably large number of dynodes, where the mean number of electrons

coming off the last dynode, and therefore the interesting values for k_n, is typically in the thousands or even millions, $e^{-\lambda_1}\frac{\lambda_n^{k_n}}{k_n!}$ quickly becomes very small, while $f_0^{(k_n)}(y)\Big|_{y=0}$ grows to extremely large values. In order to calculate $P(k_n)$ for such values of k_n, it is necessary to absorb the small factor $\frac{\lambda_n^{k_n}}{k_n!}$ into the $f_i^{(m)}$. This can be done by replacing $f_n = e^y$ with $f_n = e^{yp}$, leading to $f_n^{(m)} = f_n p^m$, and introducing a compensating factor in equation 9:

$$\begin{aligned} P(k_n) &= e^{-\lambda_1}\frac{\lambda_n^{k_n}}{k_n!}\left(\frac{1}{p}\right)^{k_n}\frac{\mathsf{d}^{k_n}}{\mathsf{d}y^{k_n}} \\ &\quad \exp(x_1\exp(x_2\exp(x_3.... \\ &\quad \exp(x_n\exp(yp))...)))\Big|_{y=0} \quad (14) \\ \text{with } x_i &:= \lambda_i e^{-\lambda_{i+1}} \end{aligned}$$

which changes $f_n^{(m)} = f_n$ in eqn 13 to $f_n^{(m)} = p^m f_n$. In order to get $p^{k_n} = \frac{\lambda_n^{k_n}}{k_n!}$ for all k_n, p must be changed at for each value k_n such that

$$p_{k_n}^{k_n} = \frac{\lambda_n^{k_n}}{k_n!}$$

So at each iteration k_n, before the $f_i^{k_n}, i < n$ are calculated using eqn 13, $f_n^{k_n}$ is set to $p_{k_n}^{k_n} = \frac{\lambda_n^{k_n}}{k_n!}$, and all the values for $f_i^{(m)}$, $m < k_n$ calculated at the previous iteration (to get $P(k_n - 1)$) need to be adjusted:

$$f_i^{(m)} \to f_i^{(m)}\left(\frac{p_{k_n}}{p_{k_n-1}}\right)^m$$

with

$$\begin{aligned} \left(\frac{p_{k_n}}{p_{k_n-1}}\right)^{k_n} &= \frac{((k_n-1)!)^{1/(k_n-1)}}{k_n} \\ &\approx (2\pi(k_n-1))^{1/(2(k_n-1))}\frac{n}{e}\frac{1}{n+1} \end{aligned}$$

Calculating the $f_i^{(m)}$ this way, eqn 14 simplifies to: $P(k_n) = e^{-\lambda_1} f_0^{k_n}$.

The binomial factor When calculating $f_0^{k_n}$, using the recursive formula 13, the factor $\binom{m}{k}$ in

$$f_i^{(m+1)} = \sum_{k=0}^{m}\binom{m}{k} f_i^{(m-k)} x_{i+1} f_{i+1}^{(k+1)}$$

can get very large for large values of $m < k_n$, while the corresponding values for $f_i^{(m)}$ get very small. To avoid the associated numerical problems, one can define $f_{a,i}$ and $f_{b,i}$ such that

$$f_i^{(m+1)} = \sum_{k=0}^{m} f_{a,i}^{(k)} x_{i+1} f_{b,i+1}^{(m+1-k)} \quad (15)$$

where

$$f_{a,i}^{(k)} = \sqrt{\binom{m}{k}} f_i^{(k)},\ f_{b,i}^{(k)} = \sqrt{\binom{m}{k-1}} f_i^{(k)}$$

This is achieved by transforming at the iteration calculating $P(k_n)$ for all $m < k_n$, $i <= n$:

$$f_{a,i}^{(m)} \to \sqrt{\frac{k_n-1}{k_n-1-m}} f_{a,i}^{(m)}$$

$$f_{b,i}^{(m)} \to \sqrt{\frac{k_n-1}{k_n-m}} f_{b,i}^{(m)}$$

Where $f_{a,i}^{(k_n)} = f_{b,i}^{(k_n)} = f_i^{(k_n)}$

The complete numerical recipe To calculate $P(k_n = r)$, calculate $P(k_n)$ subsequently for all values of $k_n = 0, \ldots, r$, starting with $k_n = 0$:

- Calculate $f_0, \ldots, f_n$, with $f_n = 1$
- $\boxed{P(0) = e^{-\lambda_1} f_0}$
- Set $f_{a,i} = f_{b,i} = f_i,\ i = 0, \ldots, n$
- Now, starting with $k_n = 1$:
  - **a)** set $f_{a,n}^{(k_n)} = f_{b,n}^{(k_n)} = f_n^{(k_n)} = \frac{\lambda_n^{k_n}}{k_n!} = f_n^{(k_n-1)}\frac{\lambda_n}{k_n}$
  - **b)** for all $m < k_n$ transform: $f_{a,i}^{(m)} \to \sqrt{\frac{k_n-1}{k_n-1-m}} f_{a,i}^{(m)}\left(\frac{p_{k_n}}{p_{k_n-1}}\right)^m \forall i \le n$ $f_{b,i}^{(m)} \to \sqrt{\frac{k_n-1}{k_n-m}} f_{b,i}^{(m)}\left(\frac{p_{k_n}}{p_{k_n-1}}\right)^m \forall i \le n$
  - **c)** calculate (for $i = n-1, \ldots, 0$) $f_i^{(k_n)} = \sum_{j=0}^{k_n-1} f_{a,i}^{(j)} x_{i+1} f_{b,i+1}^{(k_n-j)}$
  - **d)** $\boxed{P(k_n) = e^{-\lambda_1} f_0^{(k_n)}}$
  - **e)** set: $f_{a,i}^{(k_n)} = f_{b,i}^{(k_n)} = f_i^{(k_n)},\ i = 0, \ldots, n-1$
  - **f)** if $k_n < r$, increase k_n by 1 and goto **a)**

A.4 Fitting Spectra

When fitting adc spectra, the main problem is speed. The number of operations needed to calculate $P(k_n)$ using the recursive formula (eqn 13) is

$$N_{steps} \approx \sum_{i=0}^{k_n} \sum_{j=0}^{i} nj \sim k_n^3$$

which becomes absolutely prohibitive for a typical MaPMT with its gain of $\sim 3 \cdot 10^5$. Therefore, for fitting the spectra, only the exact distribution after at least $m = 4$ dynodes is calculated and then scaled by the gain of the remaining dynodes, $g_{\mathsf{rest}} = (g_{m+1} g_{m+2} \cdots g_{n-1})$. When scaling the output of the exact distribution calculated for the first m dynodes, $P_{\mathsf{exact}}(k_{m+1})$, to the final distribution, the result is smeared with a Gaussian of width σ_{scale}, taking into to account the additional spread in the distribution at each dynode:

$$\begin{aligned} \sigma_{\mathsf{scale}} &= \sqrt{k_{m+1}}\sigma_0 \\ \text{with:} & \\ \sigma_0 &= (g_{m+1} g_{m+2} \cdots g_{n-1}) \\ &\quad \cdot \left(\frac{1}{g_{m+1}} + \frac{1}{g_{m+1} g_{m+2}} + \cdots + \frac{1}{g_{m+1} \cdots g_{n-1}} \right)^{\frac{1}{2}} \end{aligned}$$

So the approximated function, $P_\sim(k_n)$ is

$$P_\sim(k_n) = \sum_{j=0}^{\infty} \frac{1}{\sqrt{2\pi}\sqrt{j}\,\sigma_0} e^{\frac{(j \cdot g_{\mathsf{rest}} - k_n)^2}{2\left(\sqrt{j}\,\sigma_0\right)^2}} P(j) \qquad (16)$$

Also, $P(k_n)$ depends on n parameters, 13 for an MaPMT (one for the mean number of photo electrons and 12 for the gain at each dynode). To make fitting large numbers of spectra feasible, this number was reduced to 2. One parameter is the mean number of p.e. coming from the photo cathode, and the other one the gain at the first dynode. Using the formula $g \propto V^k$, where V is the voltage difference over which the electron is accelerated, and k a factor typically between 0.7 and 0.8 [Hamamatsu book on Photodetectors], the gain at the other dynodes is calculated from the gain at the first dynode (using $k = 0.75$)

Finally, the spectra fitted do not show the number of photo electrons, but the output of the readout electronics (including an amplification of the signal, electronics noise and an offset) in terms of adc counts, so the function describing the spectra needs to relate the adc count with the number of electrons at the end of the dynode chain, k_n, which requires two parameters (the offset, or pedestal mean, p_0, the conversion factor, c_n of k_n to adc counts) and convolute $P(k_n)$ with a Gaussian of width σ describing the electronics noise (i is the number of adc counts):

$$F(i) = \left(\frac{1}{\sqrt{2\pi}\sigma} e^{\frac{n^2}{2\sigma^2}} \right) * \left(P\left((i - p_o)/c_n \right) \cdot c_n \right)$$

In cases where the entire spectrum is available for the fit (no losses due to events outside the dynamic range of the electronics), the number of parameters can be reduced again by setting the conversion factor c_n such that the means of the function and the fitted distribution agree.

The fit is performed as a log-likelihood fit, calculating for each bin i (which is one adc count wide) containing n_i events the binomial probability of having n_i successes in N_{all} trials with the probability of an individual success of $F(i)$, where N_{all} is the total number of events.